IEEE Access
Multidisciplinary | Rapid Review | Open Access Journal

Received May 5, 2020, accepted May 14, 2020, date of publication May 18, 2020, date of current version June 2, 2020.

Digital Object Identifier 10.1109/ACCESS.2020.2995469

Design of Discrete-Time Backstepping Sliding-Mode Control for *LCL*-Type Grid-Connected Inverter

YU WANG AND RONG-JONG WAI, (Senior Member, IEEE)
Department of Electronic and Computer Engineering, National Taiwan University of Science and Technology, Taipei 106, Taiwan
Corresponding author: Rong-Jong Wai (rjwai@mail.ntust.edu.tw)

This work was supported in part by the Ministry of Science and Technology of Taiwan under Grant MOST 108-2221-E-011-080-MY3.

ABSTRACT This study designs a discrete-time backstepping sliding-mode control (DTBSMC) method for an *LCL*-type grid-connected inverter. Firstly, the dynamic model of a discrete-time three-order system is derived, and a discrete-time backstepping control method cascading with the sliding-mode control theory is designed via Lyapunov stability verification. Moreover, the system state equation is transformed into a special form by using a time-varying mapping for overcoming the difficulty of a non-causal problem. Besides, through the recursively subsystem design for the high-order *LCL*-type inverter, the asymptotic system stability can be ensured by step-by-step virtual control designs. In addition, the proposed method can combine both the advantages of the backstepping control method and sliding-mode control theory. Therefore, the inverter system can have strong robustness under the condition of a power grid with varied grid impedances. Finally, the effectiveness of the proposed DTBSMC method is verified by numerical simulations and experimental results in comparison with a traditional proportional-resonant (PR) method and a backstepping control method.

INDEX TERMS Backstepping, sliding-mode control, discrete-time, non-causal problem, *LCL* filter, grid-connected inverter.

I. INTRODUCTION

Recently, with the increasing penetration of distributed generations (DGs), three-phase grid-connected inverters have been widely used as the interfaces between DGs and the power grid [1]. The important role of a grid-connected inverter is to provide high quality power to the power grid. Commonly, a filter is needed to reduce the switching harmonics for satisfying the requirement of low total harmonic distortion (THD). Compared with *L*-type filters, *LCL*-type filters have high harmonic attenuation ability at the switching harmonics, which permits systems to use smaller filters and increases input power quality [2], [3].

Due to the advantages of the harmonic attenuation ability, the *LCL* filter has attracted more and more attention, and a lot of linear control schemes are investigated in previous literatures. Without the limitation of a proportional-integral (PI) controller on the ac signals tracking [4], [5], linear control schemes, e.g., proportional-resonant (PR) or multi-PR controllers, are commonly used in *LCL*-type grid-connected inverters. Owing to the third-order system and resonance problem of an *LCL* filter, there exists inherent instability problem within the system. One strategy is to adopt the passive damping method, where the passive damping losses can be reduced in the certain degree by using additional reactive components in the filter circuit [6], [7]. On the other hand, many researchers have proposed active damping (AD) methods [8]–[11] without additional passive components. Liu *et al.* [8] presented a comparison of various AD methods, which were designed based on different feedbacks of four commonly used filter variables. Consequently, the grid-side current feedback AD method is selected to realize a virtual resistor in parallel with the filter capacitor. Guan *et al.* [9] proposed a dual-current active damping control strategy based on the feedback of inverter-side and grid-connected currents. Nonetheless, the equivalent virtual impedance to be simulated in series with a filter inductance will decrease the stability margin. For the stabilization and dynamic characterization, the output admittance shaping method was investigated in [10], [11], where the output admittance or impedance

The associate editor coordinating the review of this manuscript and approving it for publication was Zhilei Yao.

can be revised to satisfy the system requirements. However, the increasing penetration of DGs and the long transmission cable will make the grid impedance to be inevitable, which will change the resonant frequency of an *LCL* filter and may cause the system instability. For dealing with the grid impedance variation, some improved methods have been proposed to expand the stability region [12], [13]. In [12], an optimal design of the capacitor-current-feedback coefficient was presented by evaluating the effect of grid impedance on the gain margins, and the optimal coefficient was selected to increase the critical frequency of the stability constrain from $f_s/6$ to $f_s/2$. However, the optimal design needs to consider the prior information of the accurate value of the grid impedance. Li *et al.* [13] expressed a new method with the converter-side current feedback and the capacitor voltage-feedforward. The control method in [13] can keep the low-frequency system characteristic to be independent of the grid impedance. However, the synchronizing performance is less precise than the grid-side current feedback, and the complex compensation is necessary for the control delay. The active damping method will be helpful for damping the resonance of the *LCL* filter, but it is usually sensitive to the control delay or the parameters of the *LCL* filter and the grid impedance. Fortunately, some state-of-the-art improvements have been proposed to enhance the active damping performance [14]–[19]. In [14] and [15], modified sampling methods have been proposed for reducing the time of the control delay. Moreover, filter-based compensation methods also can be used to reduce the impact of the control delay, e.g., the infinite impulse response filter in [16] and the high-pass filter in [17]. He *et al.* [18] presented a capacitor-current proportional-integral positive feedback active damping method for addressing the problem of the negative equivalent damping resistance, and achieving high robustness to the gird impedance. Chen *et al.* [19] adopted a second-order high-pass filter on the feedback path of the capacitor current, and the improvement of the robustness against the grid impedance variation was achieved. In these methods, the damping strategy still requires to be carefully designed or an elaborate compensation strategy is necessary for enhancing the system stability performance. By considering the *LCL*-type grid-connected inverter to be a three-order nonlinear system, the nonlinear control strategies, such as the backstepping control method and the sliding-mode control (SMC) theory, are worthy to investigate.

The SMC method is one of attractive nonlinear control approaches in the power converter field due to its fast- dynamic response and strong robustness to parameter uncertainties and external disturbances [20]. In [21], a SMC method was presented for an *LCL*-type grid-connected inverter, where a sliding-surface function was formed by using the grid-current error, the capacitor-voltage error and its derivative. Wang and Wai [22] proposed a total SMC (TSMC) method for a single-phase grid-connected converter to enhance the power decoupling ability with respect to varied power coupling conditions. Because the control strategy in [22] has no reaching phase, it can ensure the robustness in the whole sliding-mode control system. However, the SMC method is an inversion control technique that requires internal dynamic stability [23]. The backstepping control method can guarantee the internal dynamic stability because of the step-by-step recursively algorithm with strictly stability condition. Each subsystem will be introduced with a virtual control law, and the error of each subsystem can be used to form the corresponding Lyapunov functions. The errors of each subsystem will achieve asymptotic convergence by each virtual control, and the nonlinear controller with global asymptotic stability can be eventually obtained [24], [25]. Although the idea of decomposed subsystems is very suitable for a three-order *LCL*-type grid-connected inverter, parameter variations and unpredictable disturbances still have obvious effect on the system performance. Hence, the combination of the SMC and backstepping control methods is adopted in this study. The backstepping sliding-mode control (BSMC) scheme can guarantee the global stability and achieve strong robustness [26], [27]. In [26], a BSMC strategy was investigated to improve the stability of the DC bus voltage for a boost converter in a DC microgrid, and the Lyapunov theory was used to prove the global asymptotic stability of the overall closed-loop system. Davila [27] presented a controller, which was designed by using the backstepping procedure, and combined the feedback linearization technique with high-order sliding-modes. In [27], the matched and unmatched disturbances can be compensated by the injection of a continuous term generated by the robust exact high-order sliding-modes differentiator. However, these methods in [26], [27] were considered under the continuous-time situation. It is common knowledge that discrete-time systems rather than the continuous-time systems are the closest for describing a real controlled system [28]. Although the linear discrete-time control system has been extensively studied in many literatures, a nonlinear discrete-time control method for an *LCL*-type grid-connected inverter has not been investigated to the same degree. What is more, there exists a non-causal problem in the design of nonlinear discrete-time control methods in [29], [30], which will make the virtual control law containing future information. The non-causal problem may lead the control law to be more complicated because it will be introduced recursively in each controller design step via the backstepping procedure, as will be discussed in Section III.

The research topic is motivated by the aforementioned discussion, and a discrete-time backstepping sliding-mode control (DTBSMC) strategy is proposed for an *LCL*-type grid-connected inverter in this study. The major contributions of the proposed DTBSMC method can be emphasized as follows: 1) the dynamic model of a discrete-time three-order *LCL*-type grid-connected inverter system is derived, and the discrete-time backstepping control method cascading with the SMC theory is designed with the discrete-time Lyapunov stability theorem. The proposed DTBSMC strategy can provide strong robustness to the grid impedance, and it is easily implemented in a digital controller; 2) the difficulty of the

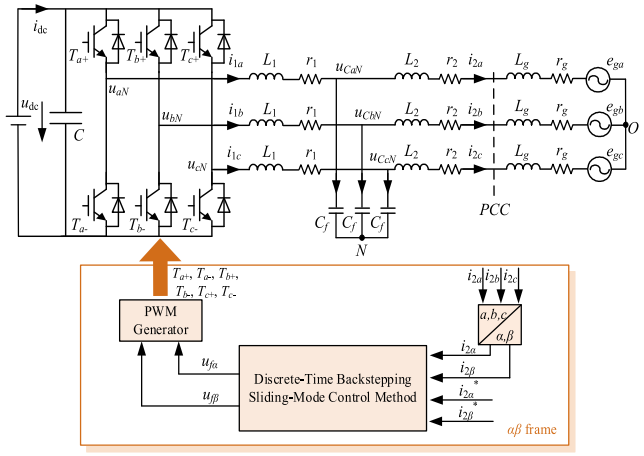

FIGURE 1. Block diagram for three-phase *LCL*-type grid-connected inverter system.

non-causal problem in the design of the proposed DTBSMC method can be overcome; 3) the proposed DTBSMC framework combines both of the merits of the backstepping control method and the SMC theory, which can guarantee global asymptotic stability without the specific design of damping methods, and 4) As our knowledge goes, there are fewer relevant researches with the proposed DTBSMC method for an *LCL*-type grid-connected inverter. The proposed DTBSMC strategy can achieve satisfactory performance and excellent control, and it can provide strong robustness under considering the grid impedance. The recursively subsystem design of the DTBSMC is also very suitable for a higher-order *LCL*-type grid-connected inverter, and it can ensure the system asymptotic stability by step-by-step virtual control designs.

This study is mainly organized into six sections. Following the introduction, the structure and the mathematical model of the *LCL*-type grid-connected inverter are described in Section II. In Section III, a discrete-time backstepping sliding-mode control method is proposed without the non-causal problem, which can achieve strong robustness and system stability. The corresponding numerical simulations and experimental results are presented in Sections IV and V, respectively. Finally, some conclusions are given in Section VI.

II. SYSTEM DESCRIPTION AND MODELING

The block diagram for a three-phase *LCL*-type grid-connected inverter is depicted in Fig. 1. As can be seen from Fig. 1, a three-phase voltage-source inverter (VSI) is connected to the power grid through an *LCL* filter. In Fig. 1, L_1 is the converter-side inductor, C_f is the filter capacitor, and L_2 is the grid-side inductor. r_1 and r_2 are equivalent series resistances (ESR) of L_1 and L_2, respectively. T_{a+}, T_{a-}, T_{b+}, T_{b+}, T_{c+}, and T_{c-} represent trigger signals for six power switches. The symbol of N is the neutral point of the filter capacitors. u_{dc} and (u_{aN}, u_{bN}, u_{cN}) denote the dc-bus voltage and the inverter AC-side terminal voltage, respectively. (i_{1a}, i_{1b}, i_{1c}) and (u_{CaN}, u_{CbN}, u_{CcN}) are output three-phase currents of the inverter and three-phase voltages of filter capacitors, respectively. The grid currents (i_{2a}, i_{2b}, i_{2c}) are controlled to be synchronized with the voltages at the point of common coupling (PCC). The weak power grid consisting of the equivalent grid inductor (L_g), the grid resistance (r_g), and ideal grid voltages (e_{ga}, e_{gb}, e_{gc}) can be modeled by the Thevenin's theorem. The model of the VSI is implemented in the stationary $\alpha\beta$ frame, and all the state variables in the *abc* frame are transformed to this basis. From Fig. 1, the dynamic model can be expressed as

$$L_G\dot{\boldsymbol{i}}_2 = \boldsymbol{u}_C - \boldsymbol{e}_g - r_G\boldsymbol{i}_2 \tag{1a}$$

$$C_f\dot{\boldsymbol{u}}_C = \boldsymbol{i}_1 - \boldsymbol{i}_2 \tag{1b}$$

$$L_1\dot{\boldsymbol{i}}_1 = \boldsymbol{D}u_{dc} - \boldsymbol{u}_C - r_1\boldsymbol{i}_1 \tag{1c}$$

where $\boldsymbol{i}_1 = [\, i_{1\alpha}\ i_{1\beta}\,]^T$ is the output current vector in α-axis and β-axis, which is transformed by (i_{1a}, i_{1b}, i_{1c}) in the *abc*-frame; $\boldsymbol{i}_2 = [\, i_{2\alpha}\ i_{2\beta}\,]^T$ is the grid current vector in α-axis and β-axis, which is transformed by (i_{2a}, i_{2b}, i_{2c}) in the *abc*-frame; $\boldsymbol{u}_C = [\, u_{C\alpha}\ u_{C\beta}\,]^T$ is the filter capacitor voltage vector in α-axis and β-axis, which is transformed by (u_{CaN}, u_{CbN}, u_{CcN}) in the *abc*-frame; $\boldsymbol{e}_g = [\, e_{g\alpha}\ e_{g\beta}\,]^T$ represents the power grid voltage vector in α-axis and β-axis, which is transformed by (e_{ga}, e_{gb}, e_{gc}) in the *abc*-frame. $\boldsymbol{D} = [\, D_\alpha\ D_\beta\,]^T$ is the duty-cycle components vector in α-axis and β-axis, which is transformed by (D_a, D_b, D_c) in the *abc*-frame and can be expressed as

$$\begin{bmatrix} D_\alpha \\ D_\beta \end{bmatrix} = \frac{2}{3}\begin{bmatrix} 1 & -\frac{1}{2} & -\frac{1}{2} \\ 0 & \frac{\sqrt{3}}{2} & -\frac{\sqrt{3}}{2} \end{bmatrix}\begin{bmatrix} D_a \\ D_b \\ D_c \end{bmatrix} \tag{2}$$

where (D_a, D_b, D_c) represent the average of the switching state function (m_a, m_b, m_c) [31], and (m_a, m_b, m_c) can be expressed as [32]

$$m_k = c_k - \frac{1}{3}\sum_{i=a,b,c} c_i, \quad k = a, b, c \tag{3}$$

where c_k represents the switching function which denotes the ON/OFF status of the devices in IGBT bridge, and it can be expressed as

$$c_k = \begin{cases} 1, & \text{if } T_{k+} \text{ is on and } T_{k-} \text{ is off} \\ 0, & \text{if } T_{k+} \text{ is off and } T_{k-} \text{ is on} \end{cases} \tag{4}$$

The terms of L_G and r_G in (1a) are defined as

$$L_G = L_2 + L_g \tag{5a}$$

$$r_G = r_2 + r_g \tag{5b}$$

According to (1), the system dynamic equation without considering parameter uncertainties and unpredictable disturbance can be obtained as [24]

$$\dddot{i}_2 = -\frac{r_1L_G + r_GL_1}{L_1L_G}\dddot{i}_2 - (\omega_r^2 + \frac{r_1r_g}{L_1L_G})\dot{i}_2 - \frac{r_1 + r_g}{L_1C_fL_G}i_2$$

$$+\frac{K_{pwm}\boldsymbol{u}_f}{L_1C_fL_G}-\frac{\boldsymbol{e}}{L_1C_fL_G}-\frac{r_1\dot{\boldsymbol{e}}_g}{L_1L_G}-\frac{\ddot{\boldsymbol{e}}_g}{L_G} \tag{6}$$

where K_{pwm} is the pulse-width-modulation (PWM) gain, and $\boldsymbol{u}_f = [\,u_{f\alpha}\ u_{f\beta}\,]^T$ is the control input; ω_r is the resonance angular frequency of the *LCL* filter, which can be expressed as

$$\omega=\sqrt{\frac{L_1+L_G}{L_1L_GC_f}} \tag{7}$$

By defining three new state variables as $\boldsymbol{x}_1=\boldsymbol{i}_2$, $\boldsymbol{x}_2=\dot{\boldsymbol{i}}_2$ and $\boldsymbol{x}_3=\ddot{\boldsymbol{i}}_2$, (6) can be rewritten as

$$\begin{cases}\dot{\boldsymbol{x}}_1=\boldsymbol{x}_2\\ \dot{\boldsymbol{x}}_2=\boldsymbol{x}_3\\ \dot{\boldsymbol{x}}_3=-\dfrac{r_1L_G+r_GL_1}{L_1L_G}\boldsymbol{x}_3-(\omega_r^2\,\boldsymbol{\mathcal{C}}\,\dfrac{r_1r_g}{L_1L_G})\boldsymbol{x}_2-\dfrac{r_1+r_g}{L_1C_fL_G}\boldsymbol{x}_1\\ \qquad+\dfrac{K_{pwm}\boldsymbol{u}_f}{L_1C_fL_G}-\dfrac{\boldsymbol{e}_g}{L_1C_fL_G}-\dfrac{r_1\dot{\boldsymbol{e}}_g}{L_1L_G}-\dfrac{\ddot{\boldsymbol{e}}_g}{L_G}\end{cases} \tag{8}$$

By applying the forward Euler discretization method [33], the discrete-time dynamic system model can be derived as

$$\begin{cases}\boldsymbol{x}_1(k+1)=\boldsymbol{x}_1(k)+T_s\boldsymbol{x}_2(k)\\ \boldsymbol{x}_2(k+1)=\boldsymbol{x}_2(k)+T_s\boldsymbol{x}_3(k)\\ \boldsymbol{x}_3(k+1)=\boldsymbol{x}_3(k)-\boldsymbol{a}_n\boldsymbol{x}_2(k)+\boldsymbol{b}_n\boldsymbol{u}_f(k)+\boldsymbol{d}_r(k)+\boldsymbol{d}_g(k)\end{cases} \tag{9}$$

where k is the sampling instant; T_s is the sampling period; $\boldsymbol{d}_r(k)=-\frac{r_1L_GT_s+r_GL_1T_s}{L_1L_G}\boldsymbol{x}_3(k)-\frac{r_1r_gT_s}{L_1L_G}\boldsymbol{x}_2(k)-\frac{r_1T_s+r_gT_s}{L_1C_fL_G}\boldsymbol{x}_1(k)$ is the vector including the terms of ESR and grid resistances; $\boldsymbol{d}_g(k)=-\frac{T_s^2+L_1C_f-r_1C_fT_s}{L_1C_fL_GT_s}\boldsymbol{e}_g(k)+\frac{2L_1-r_1T_s}{L_1L_GT_s}\boldsymbol{e}_g(k+1)-\frac{1}{L_GT_s}\boldsymbol{e}_g(k+2)$ is the grid voltage disturbance vector; $\boldsymbol{a}_n=diag(T_s\omega_r^2,\ T_s\omega_r^2)$ and $\boldsymbol{b}_n=diag\left[K_{pwm}T_s/(L_1C_fL_G)\ ,K_{pwm}T_s/(L_1C_fL_G)\right]$.

In practical applications, parameters of the *LCL* filter could be slightly different from nominal values or grid impedances could also be different from each other. Besides, considering the system with unpredictable disturbance and control delay (e.g., computation and PWM delays [13], which may be 1.5 sampling periods delay or another depended on the sampling method in the digital control), $\boldsymbol{d}_u$ and $\boldsymbol{d}_d$ will be introduced for representing the unpredictable disturbance and deviation of the control law caused by the control delay, respectively. Therefore, the system state equation in (9) can be rewritten as

$$\begin{cases}\boldsymbol{x}_1(k+1)=\boldsymbol{x}_1(k)+T_s\boldsymbol{x}_2(k)\\ \boldsymbol{x}_2(k+1)=\boldsymbol{x}_2(k)+T_s\boldsymbol{x}_3(k)\\ \boldsymbol{x}_3(k+1)=\boldsymbol{x}_3(k)-(\boldsymbol{a}_n+\Delta\boldsymbol{a}_n)\boldsymbol{x}_2(k)\\ \qquad\qquad+(\boldsymbol{b}_n+\Delta\boldsymbol{b}_n)\boldsymbol{u}_f(k)\\ \qquad\qquad+\boldsymbol{d}_r(k)+\boldsymbol{d}_g(k)+\boldsymbol{d}_d(k)+\boldsymbol{d}_u(k)\\ \qquad=\boldsymbol{x}_3(k)-\boldsymbol{a}_n\boldsymbol{x}_2(k)+\boldsymbol{b}_n\boldsymbol{u}_f(k)+\boldsymbol{d}_p(k)\end{cases} \tag{10}$$

where $\Delta\,\boldsymbol{a}_n=diag(\Delta a_{n\alpha},\ \Delta a_{n\beta})$ and $\Delta\,\boldsymbol{b}_n=diag(\Delta b_{n\alpha},\ \Delta b_{n\beta})$ represent system parameter variations; $\boldsymbol{d}_p(k)$ is the lumped uncertainty vector, which can be expressed as

$$\begin{aligned}\boldsymbol{d}_p(k)=&\,\Delta\boldsymbol{a}_n\boldsymbol{x}_2(k)+\Delta\boldsymbol{b}_n\boldsymbol{u}_f(k)\\ &+\boldsymbol{d}_r(k)+\boldsymbol{d}_g(k)+\boldsymbol{d}_d(k)+\boldsymbol{d}_u(k)\end{aligned} \tag{11}$$

As for a real circuit, the ESR is generally small, and the parameters deviations of the *LCL* filter are bounded. Moreover, the output control efforts are always limited by hardware digital/analog (D/A) ports, even for the divergence of the designed control inputs ($\boldsymbol{u}_f$). Therefore, lumped-uncertainty components in (11) can be reasonably assumed to be bounded by positive constants for a real system. Here, the lumped uncertainty vector is assumed to be bounded by $\left\|\boldsymbol{d}_p(k)\right\|<\rho$, in which $\|\cdot\|$ is the Euclidian norm, and ρ is a given positive constant.

By adopting the active damping method and considering the control delay, the active damping can be modeled as a virtual impedance, rather than as a pure resistor. However, it will shift the resonant frequency, and affect the damping performance and the system stability [12]. Note that, the proposed discrete-time backstepping sliding-mode control (DTBSMC) strategy does not need active damping mechanism, and the system stability is directly designed by the Lyapunov stability theorem. The influence of the control delay had been considered as the bounded lumped-uncertainty component ($\boldsymbol{d}_p$) in (10). Thus, the corresponding control law should be designed to satisfy the stability requirement in practical applications. Because the control delay will increase the value of $\boldsymbol{d}_p$ in a certain extent, it may enlarge the chattering phenomenon in the traditional sliding-mode control (SMC) method. Fortunately, the element in $\boldsymbol{d}_p$ caused by the control delay is limited and bounded, and the chattering phenomena can be alleviated by the design of an additional term in the proposed control framework.

III. DISCRETE-TIME BACKSTEPPING SLIDING-MODE CONTROL METHOD

In this section, the proposed discrete-time backstepping sliding-mode control (DTBSMC) method is designed to ensure the system stability and control the grid current vector ($\boldsymbol{x}_1$) to track the reference signal vector ($\boldsymbol{x}_d$), which is a purely sinusoidal signal synchronizing with the grid voltage. The control block diagram of the proposed DTBSMC strategy is depicted in Fig. 2. The three-order system model will be divided into several subsystems by the backstepping control method (in Step 1 and Step 2), and each virtual control law (α_1 and α_2) for the corresponding subsystem will be designed via the discrete-time Lyapunov stability theorem in every step. Because of the step-by-step recursively algorithm with strictly Lyapunov stability functions, this backstepping control method can guarantee the internal dynamic stability of the proposed DTBSMC strategy. The sliding-mode control method is designed in Step 3, which will ensure that the system state trajectory reaches the sliding surface, and the tracking error of the grid current can converge to zero. The final Lyapunov stability function in Step 3 is selected for

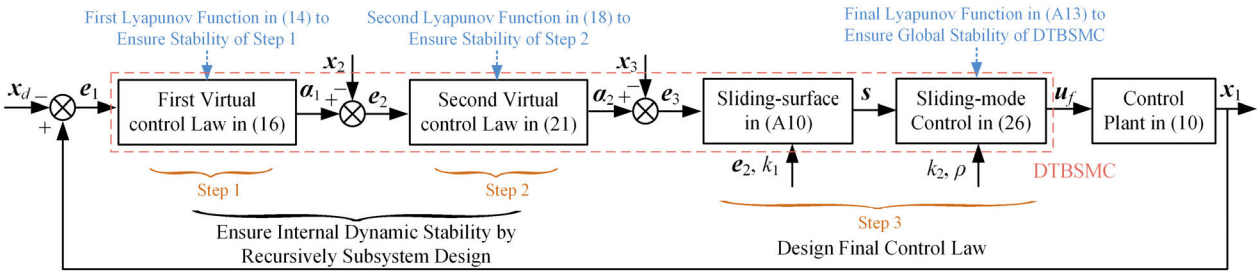

FIGURE 2. Block diagram of DTBSMC strategy.

guaranteeing the system to be global stability without using the active damping methods, even for the migration of the *LCL* filter resonance frequency or the existence of the grid impedance. The major reason of the proposed DTBSMC method without the utilization of extra damping methods is the overall control system to be directly designed via the Lyapunov stability theorem [34]. The control law of the proposed method is derived as a whole by considering system dynamic models and strictly Lyapunov stability functions, which satisfy both the requirement of the Lyapunov stability theorem in subsystems for internal dynamic stability and also the final Lyapunov stability function in Step 3 to achieve the objective of global stability. Hence, the proposed DTBSMC strategy does not need extra damping methods for compensating the system stability requirements. The detailed design process is step by step presented as follows.

Step 1: Define the tracking error vector between the controlled grid current vector ($\boldsymbol{x}_1$) and the reference signal vector ($\boldsymbol{x}_d$) as

$$\boldsymbol{e}_1(k) = \boldsymbol{x}_1(k) - \boldsymbol{x}_d(k) \tag{12}$$

where $\boldsymbol{e}_1 = [\, e_{1\alpha}\ e_{1\beta}\,]^T$ and $\boldsymbol{x}_d = [\, x_{d\alpha}\ x_{d\beta}\,]^T$. Then, the forward step of (12) can be obtained according to (10) as

$$\begin{aligned}\boldsymbol{e}_1(k+1) &= \boldsymbol{x}_1(k+1) - \boldsymbol{x}_d(k+1)\\ &= \boldsymbol{x}_1(k) + T_s\boldsymbol{x}_2(k) - \boldsymbol{x}_d(k+1)\end{aligned} \tag{13}$$

Choose the first Lyapunov function candidate [34] as

$$V_1(k) = \frac{\gamma_1}{2}\boldsymbol{e}_1^T(k)\boldsymbol{e}_1(k) \tag{14}$$

where γ_1 is a positive constant. Hence, the difference of $V_1(k)$ can be derived as

$$\begin{aligned}&\Delta V_1(k)\\ &= \frac{\gamma_1}{2}\boldsymbol{e}_1^T(k+1)\boldsymbol{e}_1(k+1) - \frac{\gamma_1}{2}\boldsymbol{e}_1^T(k)\boldsymbol{e}_1(k)\\ &= \frac{\gamma_1}{2}[\boldsymbol{x}_1(k) + T_s\boldsymbol{x}_2(k) - \boldsymbol{x}_d(k+1)]^T[\boldsymbol{x}_1(k) + T_s\boldsymbol{x}_2(k)\\ &\quad - \boldsymbol{x}_d(k+1)] - \frac{\gamma_1}{2}\boldsymbol{e}_1^T(k)\boldsymbol{e}_1(k)\\ &= \frac{\gamma_1}{2}[\boldsymbol{x}_1(k) + T_s\boldsymbol{e}_2(k) + T_s\boldsymbol{\alpha}_1(k) - \boldsymbol{x}_d(k+1)]^T\\ &\quad \times [\boldsymbol{x}_1(k) + T_s\boldsymbol{e}_2(k)\\ &\quad + T_s\boldsymbol{\alpha}_1(k) - \boldsymbol{x}_d(k+1)] - \frac{\gamma_1}{2}\boldsymbol{e}_1^T(k)\boldsymbol{e}_1(k)\end{aligned} \tag{15}$$

where $\boldsymbol{\alpha}_1(k) = [\, \alpha_{1\alpha}(k)\ \alpha_{1\beta}(k)\,]^T$ is the first virtual control law vector, and $\boldsymbol{e}_2(k) = \boldsymbol{x}_2(k) - \boldsymbol{\alpha}_1(k)$ is the second error vector between $\boldsymbol{x}_2(k)$ and $\boldsymbol{\alpha}_1(k)$. The first virtual control law vector ($\boldsymbol{\alpha}_1(k)$) in the step 1 can be given as

$$\boldsymbol{\alpha}_1(k) = [\boldsymbol{x}_d(k+1) - \boldsymbol{x}_1(k)]/T_s \tag{16}$$

By substituting (16) into (15), one can obtain

$$\Delta V_1(k) = \frac{\gamma_1}{2}T_s^2\boldsymbol{e}_2^T(k)\boldsymbol{e}_2(k) - \frac{\gamma_1}{2}\boldsymbol{e}_1^T(k)\boldsymbol{e}_1(k) \tag{17}$$

As can be seen from (17), $\Delta V_1(k)$ will be negative definite if the condition of $\boldsymbol{e}_2(k) = 0$ can be ensured. Therefore, the next step is carried out to ensure the vector of $\boldsymbol{e}_2$ for converging to zero.

Step 2: For guaranteeing the vector of $\boldsymbol{e}_2$ to converge to zero, the second Lyapunov function can be chosen as

$$V_2(k) = \frac{\gamma_2}{2}\boldsymbol{e}_2^T(k)\boldsymbol{e}_2(k) + V_1(k) \tag{18}$$

where γ_2 is a positive constant to satisfy the condition of $\gamma_1 T_s^2 < \gamma_2 < 2/T_s^2$. The ratio factor γ_1 and γ_2 here are used to introduce the physical units for the sum of Lyapunov functions to have a unified physical unit. According to (10), one can obtain the error vector of $\boldsymbol{e}_2$ as

$$\begin{aligned}\boldsymbol{e}_2(k+1) &= \boldsymbol{x}_2(k+1) - \boldsymbol{\alpha}_1(k+1)\\ &= \boldsymbol{x}_2(k) + T_s\boldsymbol{x}_3(k) - \boldsymbol{\alpha}_1(k+1)\end{aligned} \tag{19}$$

The difference of $V_2(k)$ can be derived as

$$\begin{aligned}&\Delta V_2(k)\\ &= \frac{\gamma_2}{2}\boldsymbol{e}_2^T(k+1)\boldsymbol{e}_2(k+1) - \frac{\gamma_2}{2}\boldsymbol{e}_2^T(k)\boldsymbol{e}_2(k) + \Delta V_1(k)\\ &= \frac{\gamma_2}{2}[\boldsymbol{x}_2(k) + T_s\boldsymbol{x}_3(k) - \boldsymbol{\alpha}_1(k+1)]^T\\ &\quad \times [\boldsymbol{x}_2(k) + T_s\boldsymbol{x}_3(k) - \boldsymbol{\alpha}_1(k+1)]\\ &\quad - \frac{\gamma_2}{2}\boldsymbol{e}_2^T(k)\boldsymbol{e}_2(k) + \frac{\gamma_1}{2}T_s^2\boldsymbol{e}_2^T(k)\boldsymbol{e}_2(k) - \frac{\gamma_1}{2}\boldsymbol{e}_1^T(k)\boldsymbol{e}_1(k)\\ &= \frac{\gamma_2}{2}[\boldsymbol{x}_2(k) + T_s\boldsymbol{e}_3(k) + T_s\boldsymbol{\alpha}_2(k) - \boldsymbol{\alpha}_1(k+1)]^T\\ &\quad \times [\boldsymbol{x}_2(k) + T_s\boldsymbol{e}_3(k)\\ &\quad + T_s\boldsymbol{\alpha}_2(k) - \boldsymbol{\alpha}_1(k+1)] - \frac{1}{2}(\gamma_2\\ &\quad - \gamma_1 T_s^2)\boldsymbol{e}_2^T(k)\boldsymbol{e}_2(k) - \frac{\gamma_1}{2}\boldsymbol{e}_1^T(k)\boldsymbol{e}_1(k)\end{aligned} \tag{20}$$

where $\boldsymbol{\alpha}_2(k) = [\,\alpha_{2\alpha}(k)\ \alpha_{2\beta}(k)\,]^T$ is the second virtual control law vector, and $\boldsymbol{e}_3(k) = \boldsymbol{x}_3(k) - \boldsymbol{\alpha}_2(k)$ is the third error vector between $\boldsymbol{x}_3(k)$ and $\alpha_2(k)$. The second virtual control law vector ($\alpha_2(k)$) can be designed as

$$\boldsymbol{\alpha}_2(k) = [\boldsymbol{\alpha}_1(k+1) - \boldsymbol{x}_2(k)]\,/T_s \tag{21}$$

By substituting (21) into (20), $\Delta V_2(k)$ can be derived as

$$\Delta V_2(k) = \frac{\gamma_2}{2}T_s^2\boldsymbol{e}_3^T(k)\boldsymbol{e}_3(k) - \frac{1}{2}(\gamma_2 - \gamma_1 T_s^2)\boldsymbol{e}_2^T(k)\boldsymbol{e}_2(k) - \frac{\gamma_1}{2}\boldsymbol{e}_1^T(k)\boldsymbol{e}_1(k) \tag{22}$$

The second virtual control law vector ($\alpha_2(k)$) contains the future information in the right side of (21), which will make the control law more complex as the virtual control law to be introduced recursively in each step by the backstepping design procedure. This is called a non-causal problem to be mentioned in [29], [30]. The non-causal problem will emerge when one constructs a controller for a general strict-feedback nonlinear system via the backstepping design in the discrete-time domain. This drawback can be solved by transforming the system state equation into a special form, which is suitable for the backstepping design via a time-varying mapping technique [30]. The basic idea is that if one considers the dynamic system model in (10) to be a one-step ahead predictor, and then one can transform the one-step ahead predictor into an equivalent maximum three-step ahead predictor, which can predict the future states [35]. By the time-varying mapping, the dynamic system model in (10) can be transformed as

$$\begin{cases} \boldsymbol{x}_1(k+3) = \boldsymbol{x}_1(k+2) + T_s\boldsymbol{x}_2(k+2) \\ \boldsymbol{x}_2(k+2) = \boldsymbol{x}_2(k+1) + T_s\boldsymbol{x}_3(k+1) \\ \boldsymbol{x}_3(k+1) = \boldsymbol{x}_3(k) - \boldsymbol{a}_n\boldsymbol{x}_2(k) + \boldsymbol{b}_n\boldsymbol{u}_f(k) + \boldsymbol{d}_p(k) \end{cases} \tag{23}$$

By moving one more step for $\boldsymbol{x}_1$ and $\boldsymbol{x}_2$, that is moving the state $k+1$ to $k+2$ of the first two equations in (10), the state variable $\boldsymbol{x}_1(k+1)$ and $\boldsymbol{x}_2(k+1)$ will become equivalent as

$$\begin{cases} \boldsymbol{x}_1(k+2) = \boldsymbol{x}_1(k+1) + T_s\boldsymbol{x}_2(k+1) \\ \boldsymbol{x}_2(k+2) = \boldsymbol{x}_2(k+1) + T_s\boldsymbol{x}_3(k+1) \end{cases} \tag{24}$$

Similarly, after further step, the state variable $\boldsymbol{x}_1$ of the first equation in (10) will be transformed into $\boldsymbol{x}_1(k+3)$, and it can be expressed as

$$\boldsymbol{x}_1(k+3) = \boldsymbol{x}_1(k+2) + T_s\boldsymbol{x}_2(k+2) \tag{25}$$

Thus, the state variables of $\boldsymbol{x}_1(k+1)$, $\boldsymbol{x}_2(k+1)$, and $\boldsymbol{x}_3(k+1)$ in (10) will be transformed into $\boldsymbol{x}_1(k+3)$, $\boldsymbol{x}_2(k+2)$, and $\boldsymbol{x}_3(k+1)$ as shown in (23). As a result, the non-causal problem in the derivation of the discrete-time backstepping design can be avoided when the control law is constructed based on the maximum three-step ahead predictor form. Fortunately, one can redesign the virtual control law vectors just as the previous steps, but without the causality contradiction.

Theorem 1: Consider the discrete-time dynamic system model of a three-phase *LCL*-type grid-connected inverter with a three-step ahead predictor represented by (23), if the control law vector of the proposed DTBSMC method is designed as (26), then the system stability of the designed DTBSMC method can be guaranteed.

$$\boldsymbol{u}_f(k) = \boldsymbol{b}_n^{-1}\left[\boldsymbol{F}(k) - \rho\,\mathrm{sgn}(\boldsymbol{s}(k)) - k_2\boldsymbol{s}(k) - \boldsymbol{e}_3^n(k) + k_1\boldsymbol{e}_2^n(k)\right] \tag{26}$$

where $\boldsymbol{s}(k) = \boldsymbol{e}_3^n(k) + k_1\boldsymbol{e}_2^n(k)$; $\boldsymbol{e}_2^n(k) = \boldsymbol{x}_2(k) - \boldsymbol{\alpha}_1^n(k-2)$, in which $\boldsymbol{\alpha}_1^n(k-2) = [\boldsymbol{x}_{1d}(k+1) - \boldsymbol{x}_1(k)]/T_s$; $\boldsymbol{e}_3^n(k) = \boldsymbol{x}_3(k) - \boldsymbol{\alpha}_2^n(k-1)$, in which $\boldsymbol{\alpha}_2^n(k-1) = [\boldsymbol{\alpha}_1^n(k-1) - \boldsymbol{x}_2(k)]/T_s$; $\mathrm{sgn}(\cdot)$ represents the sign function; k_1 and k_2 are positive constants; and the term of $\boldsymbol{F}(k)$ can be expressed as

$$\boldsymbol{F}(k) = -\boldsymbol{x}_3(k) + \boldsymbol{a}_n\boldsymbol{x}_2(k) - k_1\boldsymbol{x}_2(k) - k_1T_s\boldsymbol{x}_3(k) + \boldsymbol{\alpha}_2^n(k) + k_1\boldsymbol{\alpha}_1^n(k-1) \tag{27}$$

For satisfying the stability requirement, the coefficients of $0 < k_1 < \sqrt{(\gamma_2 - \gamma_1 T_s^2)/2}$ and $\|\boldsymbol{d}_p(k)\| < \rho$ should be satisfied, and the ratio factors (γ_1 and γ_2) should meet the condition of $\gamma_1 T_s^2 < \gamma_2 < 2/T_s^2$. Note that γ_1 and γ_2 adopted in V_1 and V_2 are just used to introduce the physical units so that the sum of Lyapunov functions can have a unified physical unit. Thus, both the values of γ_1 and γ_2 can be directly set to be 1. The detail stability proof is presented in the Appendix A.

In this study, a discrete-time control strategy without using the damping method has been designed. By divided into several subsystems, each virtual control laws (α_1 and α_2) have been designed with strictly discrete-time Lyapunov stability functions (V_1 and V_2) in Step 1 and Step 2 without the non-causal problem. Because of the design of strictly Lyapunov stability functions in each subsystem, the internal dynamic stability can be ensured for the discrete-time sliding-mode control in Step 3. The final control law ($\boldsymbol{u}_f$) of the proposed DTBSMC method has been designed in (26) without any requirement of the damping method. As can be seen the stability analysis in the Appendix A, the final control law ($\boldsymbol{u}_f$) can guarantee the difference of final Lyapunov function candidate (ΔV_3^n) in (A15) to be a negative-definite function, which means the system stability can be ensured even without the complex damping method. Moreover, the variation of L_G mainly affects the value of $\Delta\,\boldsymbol{b}_n$ in (10), which is namely a part of $\boldsymbol{d}_p$ as shown in (11). As can be seen in (A15), the negative-definite function can be guaranteed all the time if the condition of $\|\boldsymbol{d}_p(k)\| < \rho$ can be satisfied. By considering the value of L_G and the margin for other parts in $\boldsymbol{d}_p$ to be bounded in practice, the system stability can be ensured if a relatively larger value of ρ is selected. In order to alleviate the chattering phenomena in (26), the parameter of k_2 will be also helpful to dominate the fact that $\Delta V_3^n < 0$, which also increase the robustness to the grid impedance. As our knowledge goes, no research papers investigate the combination of backstepping control and SMC to deal with the non-causal problem for the application of the discrete-time control strategy without using additional damping methods to an *LCL*-type grid-connected inverter under a power grid with varied grid impedances.

TABLE 1. Circuit parameters and operational conditions.

Parameters	Value
Grid voltage (RMS) (e_{ga}, e_{gb}, e_{gc})	110V
Fundamental frequency f_0	60Hz
Sampling frequency f_s	10kHz
Converter-side inductance L_1 and ESR	1mH, 0.044Ω
Filter capacitor C_f	20μF
Grid-side inductance L_2 and ESR	0.45mH, 0.028Ω

IV. NUMERICAL SIMULATIONS

In order to verify the effectiveness of the proposed discrete-time backstepping sliding-mode control (DTBSMC) strategy, numerical simulations are carried out by the MATLAB/Simulink software. The circuit parameters and operational conditions are given in Table 1. The values of the converter-side and grid-side inductances (L_1 and L_2) in the three-phase inverter via the SVPWM are determined according to the design criteria in [7] and [36]. According to [7], the value of L_1 is designed as the requirement of the ripple current on L_1, and, the expression of L_1 can be expressed as

$$L_1 \geq \frac{\sqrt{3}U_{dc}}{12 f_{sw} \Delta I_2} m_r \tag{28}$$

where f_{sw} is the switching frequency; m_r is the modulation index; ΔI_2 is the ripple current and can be chosen as 25% of the rated current. When the values of $U_{dc} = 350$V, $\Delta I_2 = 25\% \times 10.6$A, and $f_{sw} = 10$kHz are selected, one can obtain that $L_1 \geq 978\mu$H. Thus, the value of L_1 is selected as 1mH in this study. The value of L_2 is designed according to the guideline in [36], where the converter harmonic voltages by Bessel functions is applied to design L_2 for reducing the grid-current harmonics and meeting the harmonic distortion limits according to the IEEE-519 standard [37]. According to [36], the expression of L_2 can be expressed as

$$L_2 \geq \frac{1}{L_1 C_f \omega_h^2 - 1}\left(L_1 + \frac{|V_{aN}(j\omega_h)|}{\omega_h \lambda_h I_2}\right) \tag{29}$$

where $|V_{aN}(j\omega_h)|$ is the output voltage of h-th order harmonic on phase-a; ω_h is the h-th order angular frequency; λ_h is the ratio of the value of filtered current at ω_h to the rated grid current. By considering the largest converter voltage harmonics occurred at the switching side-band frequency as $h = 10\text{k} - 120 = 9.88$kHz, the value of $\omega_h = 19760\pi$ rad/s can be determined. Because the order of h is higher than 33th according to IEEE-519 standard, the harmonic should be less than 0.3%, and then $\lambda_h = 0.15\%$ is taken. When the values of $L_1 = 1$mH, $C_f = 20\mu$F, $\omega_h = 19760\pi$ rad/s, $\lambda_h = 0.15\%$, and $I_2 = 10.6$A are selected, one can obtain that $L_2 \geq 0.41$mH. By considering the harmonic frequency in comparative experiment to be higher than one-sixth of the sampling frequency without damping, the value of L_2 is selected as 0.45mH in this study. Note that, filtering inductors in numerical simulations have already considered their parasitic resistances, where the corresponding values are determined according to the physical inductors used in experiments. The values of the equivalent series resistances (ESR) of the filtering inductors (L_1 and L_2) are 0.044Ω and 0.028Ω, respectively, which are measured by the *LCR* meter (*LCR*-819, Gwinstek Company). The system stability of the proposed DTBSMC strategy is directly designed by the Lyapunov stability theorem, and the influence of the ESR ($\boldsymbol{d_r}(k)$) had been considered as the bounded lumped-uncertainty component in (11). Thus, the corresponding control law can satisfy the stability requirement in practical applications. Moreover, the control coefficients of the proposed DTBSMC method are chosen according to the following guidelines. The value of k_1 is decided by considering the convergent time of the tracking error vectors, and they should satisfy the conditions of $0 < k_1 < \sqrt{(\gamma_2 - \gamma_1 T_s^2)/2}$ to ensure the Lyapunov stability requirement. The value of k_2 is selected to ensure the system stability, and it is helpful to reduce the chattering phenomena introduced by the sign function. Increasing the value of k_2 properly can dominate the fact that $\Delta V_3^n < 0$ even the worst case $\|\boldsymbol{d}_p(k)\| > \rho$ happens, which means that the parameter ρ could be conservatively selected to avoid increasing the chattering phenomena caused by the term of $\rho \text{sgn}(s(k))$. The parameter ρ can be roughly determined by the limited range of the possible occurrence of parameter variations and external disturbance. By considering the value of the *LCL* filter deviating 20% and the grid impedance to be 10mH, the estimated value of $||d_p||$ can be calculated according to (11). By using the parameters in Table 1, one can roughly obtain the theoretical bound value of $||d_p||$ to be about 1.47×10^9. However, the selection of a large value ρ will cause the control effort with serious chattering phenomena and deteriorate the corresponding control performance. Fortunately, the selection of a large value k_2 is helpful for reducing the value of ρ in the proposed methodology because the term - $k_2\, \boldsymbol{s}(t)$ in (26) will dominate the fact of $\Delta V_3^n < 0$. By considering a better transient control performance as well as the requirement of stability, and combining the possible occurrence of uncertainties through numerical simulations, the values of $k_1 = 0.1, k_2 = 50$, and $\rho = 30$ via the trial-and-error procedure are selected in the proposed DTBSMC method.

In order to illustrate the superiority of the proposed DTBSMC method, numerical simulations of a traditional quasi proportional-resonant (PR) method in [38], and a backstepping control method in [24] are compared in this study. The intention of this study is not to draw the conclusion that the non-linear methods are definitely better than linear control methods, but to adopt a non-linear control structure, which combines the merits of the backstepping control method and the SMC theory, to design a discrete-time control strategy without using additional damping methods. The linear control structure, which adopts the PR controller commonly used in the control strategy without using additional damping methods, is taken as a contrast to show the robustness of

the proposed DTBSMC strategy with respect to the grid impedance. Similarly, another non-linear control structure, which adopts the backstepping structure, is also compared with the proposed DTBSMC strategy. The PR controller can be expressed as

$$G_{PR}(s) = k_{rp} + \frac{2k_{ri}\omega_b s}{s^2 + 2\omega_b s + \omega_0^2} \tag{30}$$

where s is the Laplace operator; k_{rp} and k_{ri} are the proportional gain and the resonance gain, respectively; ω_0 and ω_b are the resonance frequency and the bandwidth of the resonance controller, respectively. The discrete form of (26) can be expressed as [38]

$$G_{PR}(z) = k_{rp} + \frac{2k_{ri}\omega_b T_s(z-1)}{z^2 + z(\omega_0^2 T_s^2 + 2\omega_b T_s - 2) - 2\omega_b T_s + 1} \tag{31}$$

where z is the z-transform operator. $\omega_0 = 120\pi$ rad/s is the fundamental angular frequency, and $\omega_b = 1.2\pi$ rad/s is selected to deal with a typical $\pm 1\%$ variation of the grid fundamental frequency. $k_{rp} = 4$ and $k_{ri} = 80$ are chosen by the root locus method as the design guideline in [38].

Ge *et al.* [24] adopted the backstepping control method for an *LCL*-type converter to be used as an active power filter. The control structure of the backstepping control method in [24] is implemented into three steps, and each step has a corresponding Lyapunov function for ensure the stability of each control law in every step. Finally, the tracking errors in each step will asymptotically converge to zero, and the grid current can be ensured to track the reference signal. Hence, the idea of the backstepping control method in [24] is adopted in this study as a comparative algorithm. By following the design steps in [24], the control structure is also divided into three steps to eventually ensure the grid current to be controlled. In addition, the backstepping control method is also discretized in this study for a fair comparison with the proposed DTBSMC strategy. The design procedure of the backstepping control method is similar to the design steps in the Appendix A, but without the SMC method in Step A3. The control law (u_{fb}) of the backstepping control method can be expressed as

$$\boldsymbol{u}_{fb}(k) = \boldsymbol{b}_n^{-1}\left[-\boldsymbol{x}_3(k) + \boldsymbol{a}_n\boldsymbol{x}_2(k) + \boldsymbol{\alpha}_2^n(k)\right] \tag{32}$$

The detail derivation of (30) can be referred to Appendix B. In this study, the focus is to design a control strategy without using the damping method, and keep the strong robustness to the grid impedance. A common proportional-resonant (PR) controller without the damping method is adopted for comparisons in this study, and it belongs to a linear control structure. The PR controller also can ensure the system stability without using the damping method, but only in the case that the initial value of the *LCL* resonance frequency is higher than the critical frequency ($f_s/6$) for the grid-side current feedback [39]. More importantly, the proposed DTBSMC method does not use extra damping method, and can ensure the system stability without the limit of the critical frequency, whatever the value of the *LCL* resonance frequency changes.

The proposed DTBSMC method can guarantee the system stability without using the complex active damping strategy. Although the PR controller can also ensure stability without damping if the *LCL* filter resonance frequency is higher than the critical resonance frequency, which is one-sixth of the sampling frequency (f_s), the strong robustness to the grid impedance will be hardly kept. In Fig. 3, three control methods are carried out under an ideal power grid, where the grid impedance is zero. The resonance frequency of the *LCL* filter in Table 1 is 2kHz, which is larger than $f_s/6$ (1.6kHz). It can be seen from Fig. 3(a)-(c) that all these control methods can keep the grid current with a very good sinusoidal waveform under the ideal power grid. In Fig. 3(c), the total-harmonic-distortion (THD) value of the proposed DTBSMC method is 1.21% to be the lower one. The proposed DTBSMC strategy can provide a high-quality current to the power grid, and the system stability can be guaranteed with the control design by the Lyapunov stability theorem in Section III.

For verifying the robustness of the proposed DTBSMC strategy under the existence of the grid impedance, numerical simulations with different grid impedances (2mH and 3mH) are depicted in Figs. 4 and 5, respectively. In Fig. 4, the grid impedance is increased to 2mH, and the resonance frequency of the *LCL* filter is declined to 1.3kHz, which is smaller than $f_s/6$ (1.6kHz). As can be seen from Fig. 4(a), the grid current caused by the PR method is hardly to keep stability owing to the increased grid impedance. Although the backstepping control method still can guarantee the system stability in Fig. 4(b), the THD value of the grid current is increased to be 2.74%. When the grid impedance continues to increase to 3mH, the THD value of the grid current is further deteriorated to 3.04%, which is increased more than 125% comparing with the one under ideal power grid in Fig. 3(b). In contrast, because of the strong robustness of the proposed DTBSMC strategy, the grid current still can keep desirable quality when the grid impedance exists, and its THD values in Fig. 4(c) and Fig. 5(c) are only 1.86% and 1.97%, respectively. Compared with Fig. 5(c) and the one under ideal power grid in Fig. 3(c), the increment of the THD value is reduced almost 55% than the backstepping control method in Fig. 5(b). According to the analysis of the Lyapunov stability theorem in Section III, the proposed DTBSMC strategy can guarantee the strong robustness, and the stability is independent of the varied grid impedance. Therefore, the system performance under wide range grid impedance variation from 1mH to 10mH is depicted in Fig. 6. Comparing with the performance of the backstepping control method in 10mH grid impedance, the increment of the THD value of the proposed strategy can be reduced more than 64%. Even though the grid impedance has large variations, the proposed DTBSMC method still can guarantee the global asymptotic stability as well as the desirable current quality.

In order to examine the influence of the values of ρ and k_2 on the control chattering phenomena, numerical simulations

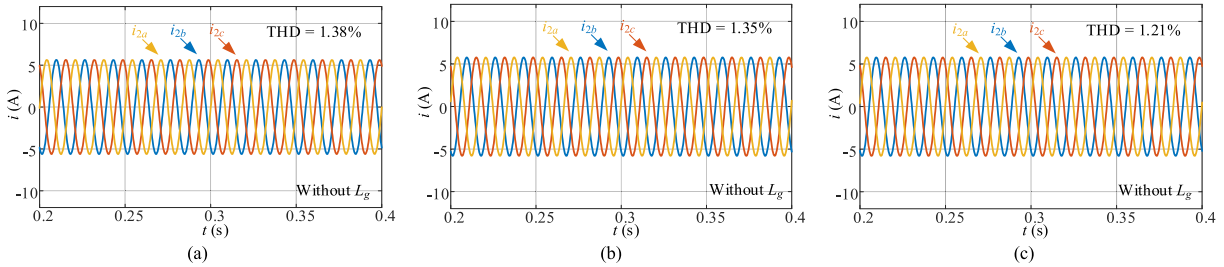

FIGURE 3. Numerical simulations under ideal power grid. (a) PR method in [38]. (b) Backstepping control method in [24]. (c) Proposed DTBSMC method.

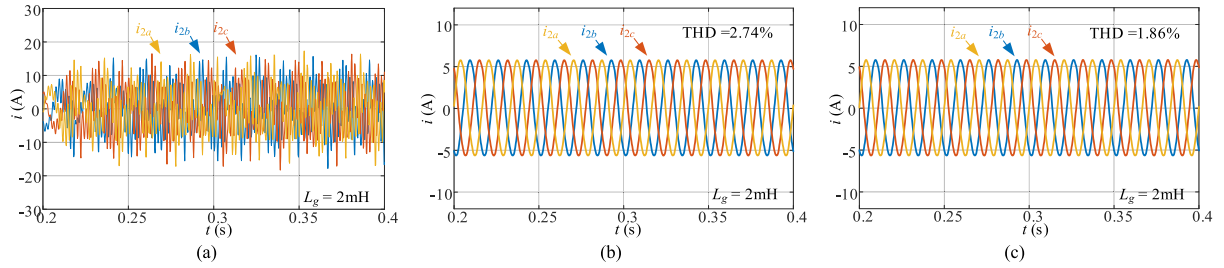

FIGURE 4. Numerical simulations under 2mH grid impedance. (a) PR method in [38]. (b) Backstepping control method in [24]. (c) Proposed DTBSMC method.

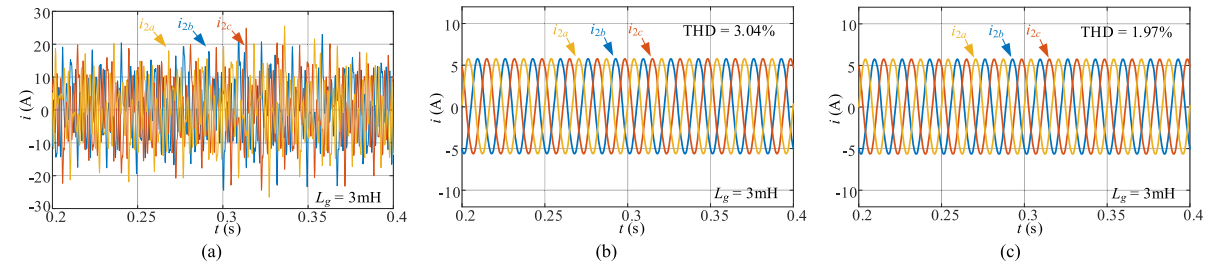

FIGURE 5. Numerical simulations under 3mH grid impedance. (a) PR method in [38]. (b) Backstepping control method in [24]. (c) Proposed DTBSMC method.

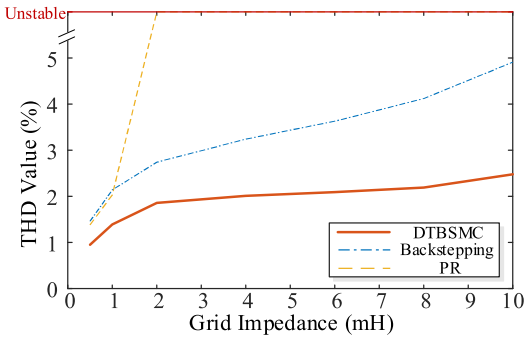

FIGURE 6. THD values of grid current under various grid impedance.

of the three-phase LCL-type grid-connected inverter system operated from Case 1 to Case 4 are given in Fig. 7. In Fig. 7, the values of ρ and k_2 are respectively selected as $\rho = 1\times10^6$ and $k_2 = 0$ for Case 1; $\rho = 8\times10^6$ and $k_2 = 0$ for Case 2; $\rho = 2\times10^7$ and $k_2 = 0$ for Case 3; $\rho = 30$ and $k_2 = 50$ for Case 4. As can be seen from Fig. 7(a), the system cannot keep stability because only the value of ρ is considered and its value is too small. By gradually increasing the value of ρ for Case 2 and Case 3 in Fig. 7(b), the system can achieve the stable control objective. Unfortunately, the control chattering phenomena are accordingly augmented with the increasing value of ρ, and the value of THD is increased to 18.54%. As for Case 4 in Fig. 7(b), owing to the parameter of k_2 is considered, a smaller value of ρ can be selected and the corresponding chattering phenomena can be alleviated.

Remark 1: In general, the PR controller via the selection of appropriate control parameters also can ensure the system stability without using the damping method if the *LCL* filter resonance frequency is higher than the critical resonance frequency, which is one-sixth of the sampling frequency (f_s). However, the strong robustness to the grid impedance will be hardly kept by the PR controller under the variation of the resonance frequency to be lower than this critical resonance frequency. When the *LCL* filter resonance frequency is smaller than $f_s/6$ owing to the increased grid impedance,

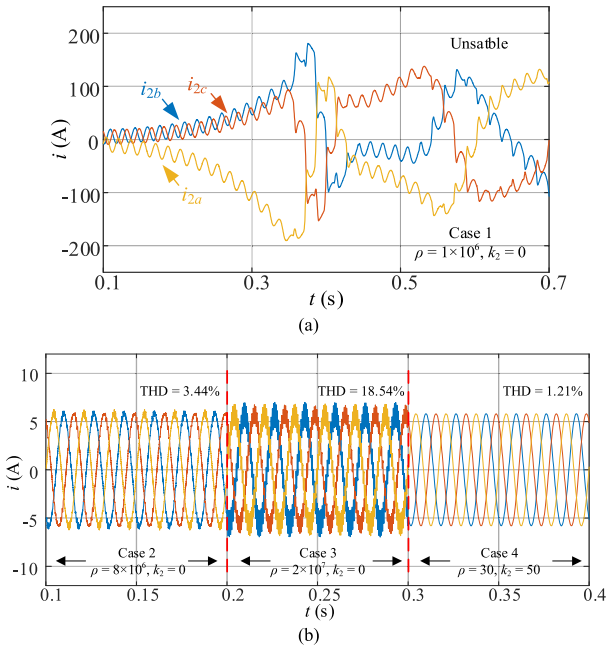

FIGURE 7. Numerical simulations of proposed DTBSMC method under different values of ρ and k_2.

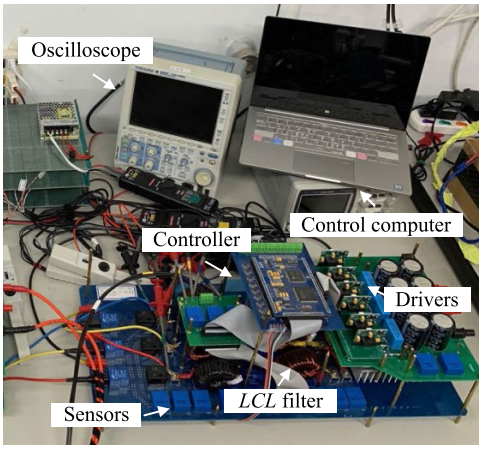

FIGURE 8. Photograph of experimental prototype.

the PR controller without the damping method cannot keep the system stability as shown in Fig. 4(a). By comparing Fig. 4(a) with Fig. 4(c), the proposed DTBSMC method without any extra damping strategy can ensure the system stability no matter where the resonance frequency locates.

V. EXPERIMENTAL RESULTS

An experimental prototype has been constructed as shown in Fig. 8 to verify the effectiveness of the proposed discrete-time backstepping sliding-mode control (DTBSMC) scheme. The control algorithm is implemented by a digital signal processor (DSP) and a field-programmable gate array (FPGA) digital microcontroller, where the DSP (TMS320F28335) is a main algorithm controller, and the FPGA (XC3S400)

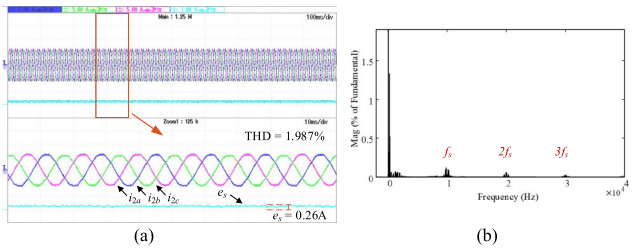

FIGURE 9. Experimental results of PR method in [38] under ideal grid. (a) Grid current responses. (b) Spectrum of grid current.

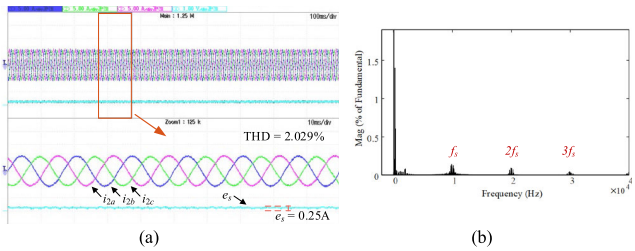

FIGURE 10. Experimental results of backstepping control method in [24] under ideal grid. (a) Grid current responses. (b) Spectrum of grid current.

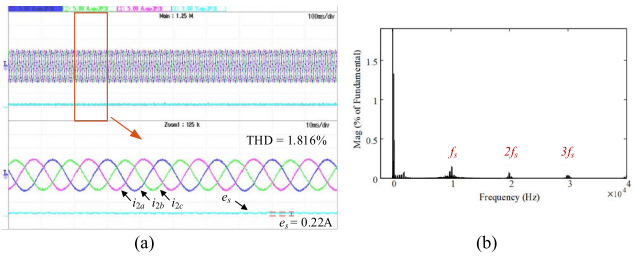

FIGURE 11. Experimental results of proposed DTBSMC method under ideal grid. (a) Grid current responses. (b) Spectrum of grid current.

is an assistant controller for implementing the pulse-width-modulation (PWM), sampling signal processing, and fault protection, etc. The experimental circuit parameters and operational conditions are the same as Table 1. By considering the practical situation, the actual parameters of the *LCL* filter could be slightly different from nominal values in Table 1.

Although the derivation of the proposed DTBSMC strategy has many equations in Section III, most of them are intermediate variables or the derivations of the stability for each step. The overall control law of the proposed DTBSMC strategy is $\boldsymbol{u}_f$ (in (26)), which can be easily implemented in a DSP. Only grid-current sensors are required for sampling the grid currents ($\boldsymbol{x}_1$) and send them to the DSP. Then, the final DTBSMC law ($\boldsymbol{u}_f$) in (26) can be calculated, where the virtual control law (α_1 and α_2) and sliding-surface ($\boldsymbol{s}$) are just intermediate variables, and the actual calculation of $\boldsymbol{u}_f$ in the DSP depends only on $\boldsymbol{x}_1$ and the current reference signal ($\boldsymbol{x}_d$). Moreover, the control law will be sent to the program of space-vector pulse-width-modulation (SVPWM) in a FPGA digital microcontroller for generating corresponding drive signals.

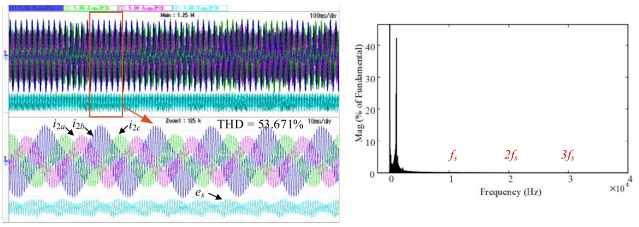

FIGURE 12. Experimental results of PR method in [38] under 1.92mH grid impedance. (a) Grid current responses. (b) Spectrum of grid current.

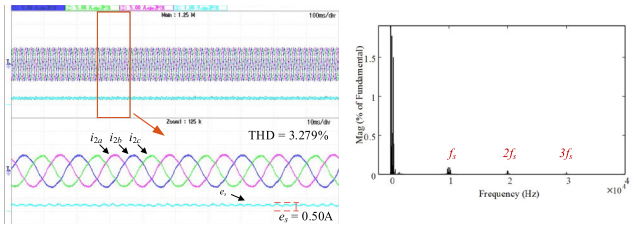

FIGURE 13. Experimental results of backstepping control method in [24] under 1.92mH grid impedance. (a) Grid current responses. (b) Spectrum of grid current.

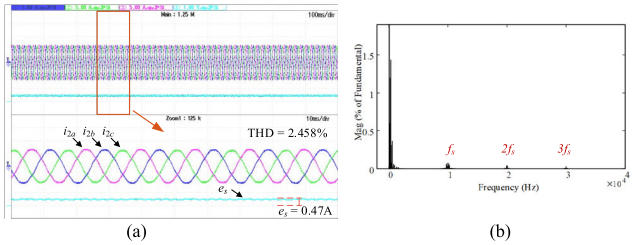

FIGURE 14. Experimental results of proposed DTBSMC method with 1.92mH grid impedance. (a) Grid current responses. (b) Spectrum of grid current.

Figure 9-11 shows the experimental results of the traditional proportional-resonant (PR) method in [38], the backstepping control method in [24], and the proposed DTBSMC method under an ideal power grid, where the experimental conditions are the same as the ones in Fig. 3. In Fig. 9-11, all of the three control methods can ensure the system stability under the ideal power grid, and all the grid currents can be kept in good quality. The tracking error index can be defined as $e_s = \sqrt{e_{1\alpha}^2 + e_{1\beta}^2}$, where $e_{1\alpha}$ and $e_{1\beta}$ are the tracking errors between the grid currents and its references in the stationary $\alpha\beta$ frame, respectively. The maximum value of e_s for the proposed DTBSMC method is 0.22A, which is 15% and 12% smaller than the PR method and backstepping control method in Fig. 9(a) and 10(a), respectively. As can be seen from Fig. 11, the proposed DTBSMC strategy can provide a high quality current to the power grid, where the corresponding total-harmonic-distortion (THD) value is 1.816% to be the lowest one of the three control methods.

In order to illustrate the strong robustness of the proposed DTBSMC strategy, experimental current responses and spectrums with 1.92mH grid impedances for all three methods are depicted in Fig. 12-14. Because the varied resonance frequency is lower than the critical resonance frequency (f_s/6) attributed to the grid impedance, the PR method in Fig. 12 is hard to keep stability any more. Although the total inductance of the *LCL* filter is only about 1.5mH, the resonance frequency will migrate to about 1.342kHz (lower than the f_s/6) by considering the 20μF filter capacitor and the 1.92mH grid impedance. As can be seen from Fig. 12, the resonance still occurs, even the practical situation contains resistive components (e.g., ESR). In Fig. 12(b), the resonance frequency is the same about 1.3kHz, which is accordance with the theoretical analysis. The similar result also can be seen from the simulation in Fig. 4(a), where the grid impedance is 2mH. As can be seen from Fig. 14, the proposed DTBSMC method still can guarantee the system stability, even though the grid impedance is increased to be 1.92mH. Moreover, the grid current caused by the proposed DTBSMC method can be kept in desirable performance, where the THD value is 2.458%. Although the backstepping control method also can keep the system stability as shown in Fig. 13, the grid impedance has more serious impact on it. The corresponding THD value in Fig. 13(b) is 3.279%, where the increment is 48% larger than the proposed strategy, and the ratio will continue to grow as the gird impedances increase. Similar to numerical simulations in Figs. 4-6, owing to the advantages of the backstepping control structure and the sliding-mode control theory, the proposed DTBSMC scheme can have strong robustness to the variations of grid impedances. As can be seen from Fig. 6, the THD value of the proposed DTBSMC strategy is 1.86% as the grid impedance is 2mH. Although the value of the grid impedance is increased to be 10mH, the increase of the THD value is relatively limited, and its THD value is only 2.48%. Note that, inductors in numerical simulations are ideal devices and their values are fixed. However, inductors in the experiments are non-ideal and varied, and the inductance permeability will be decreased as the current is increased. By comparing Fig. 14 with Fig. 6, the THD value of the grid current in the experimental result is larger than the one in the numerical simulation.

Figure 15 shows the experimental results under an unbalanced power grid for all the three methods, where the grid voltage drops 10% and 20% in phase-B and phase-C, respectively. The definition of m_u is the unbalanced current index, and it can be represented as

$$m_u = \frac{Max(i_{2a}, i_{2b}, i_{2c}) - Min(i_{2a}, i_{2b}, i_{2c})}{Avg(i_{2a}, i_{2b}, i_{2c})} \times 100\% \quad (33)$$

where $Max(\cdot)$, $Min(\cdot)$ and $Avg(\cdot)$ represent the maximum, minimum and average root-mean-square (RMS) current of the three-phase grid currents (i_{2a}, i_{2b}, i_{2c}), respectively. As can be seen from Fig. 15(b), the unbalanced current index (m_u) of the backstepping control method and the PR method is 8.3% and 3.7%, respectively. Owing to the characteristic of strong robustness, the grid current of the proposed

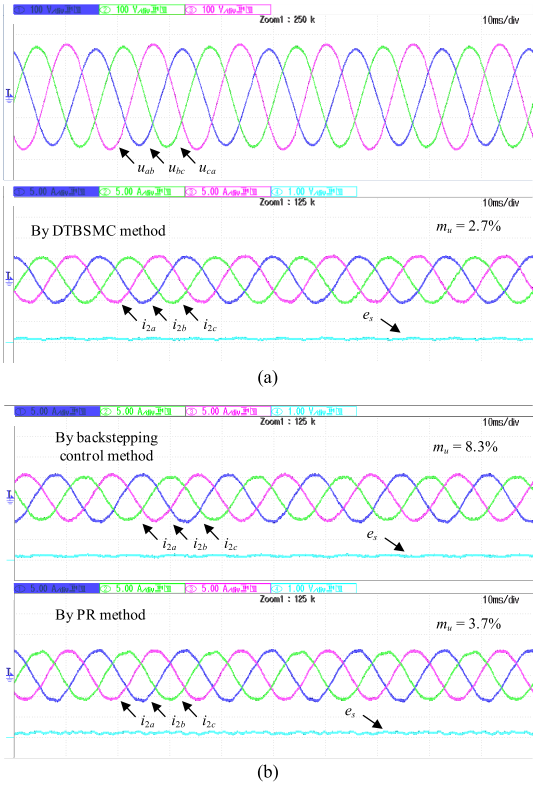

FIGURE 15. Experimental results with unbalanced power grid. (a) Proposed DTBSMC method. (b) Backstepping control method in [24] and PR method in [38].

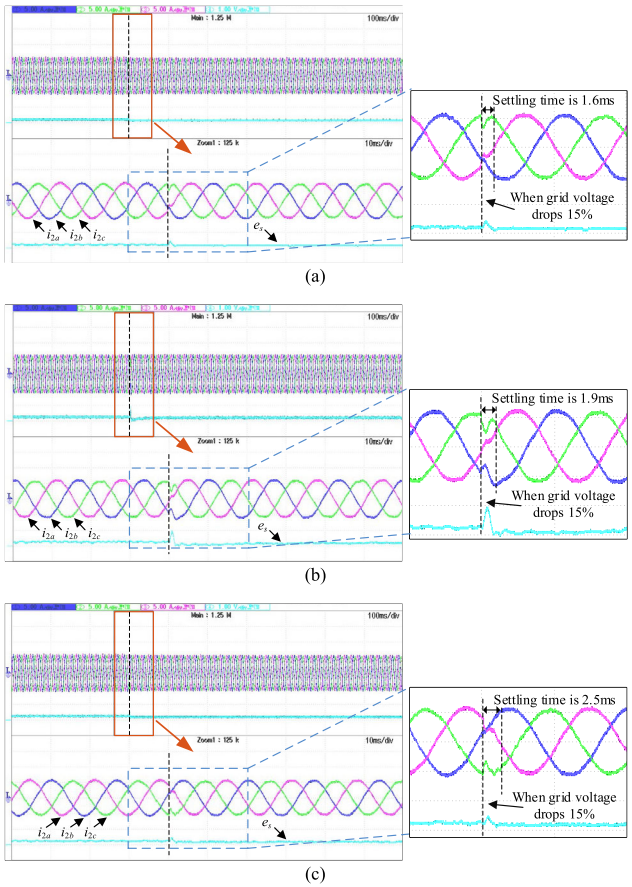

FIGURE 16. Experimental results with grid voltage dip. (a) Proposed DTBSMC method. (b) PR method in [38]. (c) Backstepping control method in [24].

DTBSMC method still can maintain desirable sinusoidal waveforms in despite of the unbalanced grid voltage. The unbalanced current index (m_u) of the proposed DTBSMC strategy in Fig. 15(a) is 2.7%, which is 27% and 67% smaller than the PR method and the backstepping control method shown in Fig. 15(b), respectively.

Figure 16 shows the experimental results of the proposed DTBSMC method, the PR method in [38] and the backstepping control method in [24] as the grid voltage to be suddenly dropped 15%. As for the occurrence of the grid voltage variation, the maximum fluctuation of the tracking error index (e_s) by the PR method is about 1A in Fig. 16(b); the one by the proposed DTBSMC method in Fig. 16(c) is reduced almost 50%. As can be seen from Fig. 16, the grid voltage dip has very slight impact on the grid current of the proposed DTBSMC method. Moreover, the grid current fluctuation of the proposed DTBSMC method can be stabilized within about 1.6ms, which is 16% and 36% faster than the PR method and the backstepping control method in Fig. 16(b) and 16(c), respectively.

In order to verify the dynamic response, the experimental results of the proposed DTBSMC method, the PR method in [38] and the backstepping control method in [24] under the variations of current references are depicted in Fig. 17. The step change of the current reference is from 6 A to 4 A. By comparing with the PR method and the backstepping control method in Fig. 17(b) and 17(c), the proposed DTBSMC strategy can have a very fast dynamic performance in Fig. 17(a), and the grid current can track the changed reference rapidly in almost 1.7ms, which is 19% and 57% faster than the PR method and backstepping control method, respectively. Owing to the step-by-step recursively algorithm with strictly stability condition, the backstepping control architecture can ensure all the state variables of the SMC method to be internal dynamic stability. Therefore, the characteristic of fast-dynamic response in SMC still can be retained because the error of state variables will converge exponentially to zero once the system state trajectory reaches the sliding surface. The experimental performance comparisons of three control methods are summarized in Table 2. As can be seen from Table 2, the proposed DBSMC strategy indeed yields superior performance than the PR method in [38] and the backstepping control method in [24].

The proposed DTBSMC method can achieve the strong robustness to the grid impedance, and does not need the additional carefully design for the damping strategy. By considering the dynamic system model, the control system is directly designed as the requirement of the Lyapunov stability theorem [34]. Although the derivation contains many equations,

TABLE 2. Experimental performance comparisons of different methods.

Operational conditions	PR method in [38]	Backstepping control method in [24]	**Proposed DTBSMC method**
THD under ideal grid	1.987%	2.029	**1.816%**
THD under 1.92mH grid impedance	Unstable	3.279%	**2.458%**
Tracking error index (e_s) under 1.92mH grid impedance	Unstable	0.50A	**0.47A**
Unbalanced current index (m_u) under unbalanced grid	3.7%	8.3%	**2.7%**
Settling time under grid voltage dip	1.9ms	2.5ms	**1.6ms**
Settling time under current reference variation	2.1ms	4ms	**1.7ms**
Execution time	13μs	14.25μs	**16.25μs**

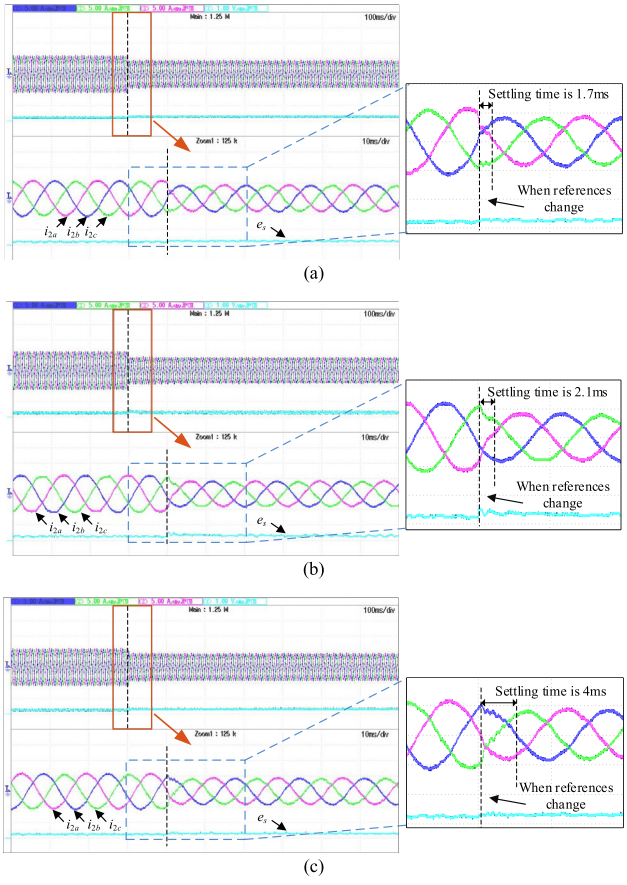

FIGURE 17. Experimental results with step change of current reference. (a) Proposed DTBSMC method. (b) PR method in [38]. (c) Backstepping control method in [24].

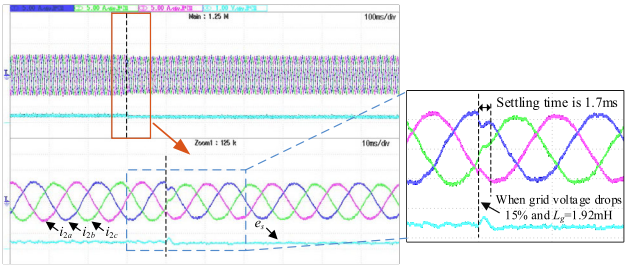

FIGURE 18. Experimental results of proposed DTBSMC method under grid voltage dip with 1.92mH grid impedance.

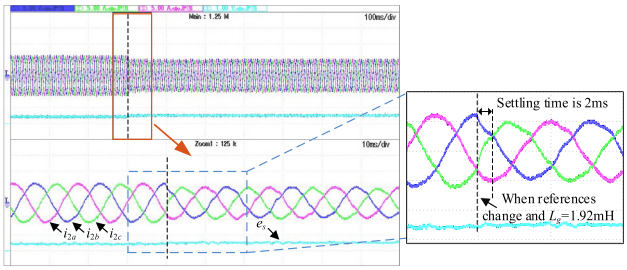

FIGURE 19. Experimental results of proposed DTBSMC method under step change of current reference with 1.92mH grid impedance.

most of them are intermediate variables and the stability derivation by following the Lyapunov stability theorem. What is more, the control law is derived in the discrete-time, which will make the form of the equation complex, but it is more suitable for the digital signal processor. Eventually, only the control law in (26) is finally implemented to the control object. The execution times of each control method are also provided in Table 2. As can be seen from Table 2, the execution times of the PR method in [38], the backstepping control method in [24], and the proposed DTBSMC method are 13μs, 14.25μs and 16.25μs, respectively. Although the execution time of the proposed DTBSMC method is 25% larger than the one of the PR controller, the stronger robustness and better performance can be achieved by the proposed DTBSMC method. In addition, by considering the advanced computing power of the microprocessor and the 100μs sampling time, the execution time of the proposed DTBSMC method is still acceptable.

In order to test the performance of the proposed DTBSMC strategy with considering the grid impedance, experimental results with 1.92mH grid impedance under the grid voltage drip and the step change of current reference are depicted in Figs. 18 and 19, respectively. The grid voltage is dropped 15% in Fig. 18, and the reference current is changed from

6A to 4A in Fig. 19. Compared with the performances in Figs. 16(a) and 17(a), the existence of the grid impedance will increase the settling time. Fortunately, the corresponding impact is still slight owing to the strong robustness of the proposed DTBSMC strategy.

VI. CONCLUSIONS

This study has successfully designed a discrete-time backstepping sliding-mode control (DTBSMC) method for an *LCL*-type grid-connected inverter. Through the step-by-step virtual control designs, the proposed DTBSMC strategy can ensure the system asymptotic stability. Based on the discrete-time Lyapunov stability theory, a suitable control law is derived to guarantee the accurate control and global stability of the overall closed-loop system. Moreover, a detailed design procedure is presented for overcoming the difficulty of a non-causal problem. What is more, the proposed DTBSMC method combines both advantages of the backstepping control method and the sliding-mode control theory. Therefore, the internal dynamic stability can be ensured by the several subsystems design. In addition, the proposed DTBSMC scheme can realize the features of good dynamic performance and strong robustness to the grid impedance without the specific design of damping strategy. Compared with the traditional proportional-resonant (PR) method and the backstepping control method in experiments, the total-harmonic-distortion (THD) value of the proposed DTBSMC method is 2.458%, where the increment of the THD value is reduced 48% when the grid impedance is 1.92mH. Furthermore, the settling time under the reference variation of the proposed DTBSMC strategy is 19% and 57% faster than the traditional PR method in [38] and the backstepping control method in [24], respectively. Numerical simulations and experimental results are provided to verify the effectiveness of the proposed DTBSMC strategy.

APPENDIX A

The design procedure and stability verification of the proposed DTBSMC method in Theorem 1 are represented as follows.

Step A1: The first Lyapunov function candidate is chosen as the same as (14). By considering the tracking error vector ($\boldsymbol{e}_1$) in (12), the difference of $V_1(k)$ can be derived as

$$\begin{aligned}\Delta V_1^n(k) = \frac{\gamma_1}{2}&\left[\boldsymbol{x}_1(k)+T_s\boldsymbol{e}_2^n(k)+T_s\boldsymbol{\alpha}_1^n(k-2)-\boldsymbol{x}_d(k+1)\right]^T\\ &\times\left[\boldsymbol{x}_1(k)+T_s\boldsymbol{e}_2^n(k)+T_s\boldsymbol{\alpha}_1^n(k-2)-\boldsymbol{x}_d(k+1)\right]\\ &-\frac{\gamma_1}{2}\boldsymbol{e}_1^T(k)\boldsymbol{e}_1(k)\end{aligned}\tag{A1}$$

where $\boldsymbol{e}_2^n(k) = \boldsymbol{x}_2(k) - \boldsymbol{\alpha}_1^n(k-2)$ is the new second error vector because of the two-step ahead predictor form of $\boldsymbol{x}_2$ in (23). In order to achieve the negative-definite form of $\boldsymbol{e}_1$ in (A1), a new first virtual control law vector ($\boldsymbol{\alpha}_1^n$) in the step A1 can be given as

$$\boldsymbol{\alpha}_1^n(k-2) = \left[\boldsymbol{x}_{1d}(k+1) - \boldsymbol{x}_1(k)\right]/T_s\tag{A2}$$

which can be equivalently expressed as

$$\begin{aligned}\boldsymbol{\alpha}_1^n(k) &= \left[\boldsymbol{x}_{1d}(k+3) - \boldsymbol{x}_1(k+2)\right]/T_s\\ &= \left[\boldsymbol{x}_{1d}(k+3) - \boldsymbol{x}_1(k+1) - T_s\boldsymbol{x}_2(k+1)\right]/T_s\\ &= \left[\boldsymbol{x}_{1d}(k+3) - \boldsymbol{x}_1(k) - 2T_s\boldsymbol{x}_2(k) - T_s^2\boldsymbol{x}_3(k)\right]/T_s\end{aligned}\tag{A3}$$

By substituting (A2) into (A1), one can obtain

$$\Delta V_1^n(k) = \frac{\gamma_1}{2}T_s^2\boldsymbol{e}_2^{nT}(k)\boldsymbol{e}_2^n(k) - \frac{\gamma_1}{2}\boldsymbol{e}_1^T(k)\boldsymbol{e}_1(k)\tag{A4}$$

The difference of $V_1(k)$ in (A4) is similar to the one in (17). In order to force (A4) to be a negative-definite function, the next step is to guarantee the vector of $\boldsymbol{e}_2^n$ for converging to zero.

Step A2: For ensuring the second error vector ($\boldsymbol{e}_2^n$) can converge to zero, one can choose a new second Lyapunov function candidate as

$$V_2^n(k) = \frac{\gamma_2}{2}\boldsymbol{e}_2^{nT}(k)\boldsymbol{e}_2^n(k) + V_1(k)\tag{A5}$$

Therefore, the difference of $V_2^n(k)$ can be derived as

$$\begin{aligned}\Delta V_2^n(k) = \frac{\gamma_2}{2}&\left[\boldsymbol{x}_2(k)+T_s\boldsymbol{e}_3^n(k)+T_s\boldsymbol{\alpha}_2^n(k-1)-\boldsymbol{\alpha}_1^n(k-1)\right]^T\\ &\times\left[\boldsymbol{x}_2(k)+T_s\boldsymbol{e}_3^n(k)+T_s\boldsymbol{\alpha}_2^n(k-1)-\boldsymbol{\alpha}_1^n(k-1)\right]\\ &-\frac{1}{2}(\gamma_2-\gamma_1T_s^2)\boldsymbol{e}_2^{nT}(k)\boldsymbol{e}_2^n(k)-\frac{\gamma_1}{2}\boldsymbol{e}_1^T(k)\boldsymbol{e}_1(k)\end{aligned}\tag{A6}$$

where $\boldsymbol{e}_3^n(k) = \boldsymbol{x}_3(k) - \boldsymbol{\alpha}_2^n(k-1)$ is the new third error vector. A new second virtual control law vector can be designed as

$$\boldsymbol{\alpha}_2^n(k-1) = \left[\boldsymbol{\alpha}_1^n(k-1) - \boldsymbol{x}_2(k)\right]/T_s\tag{A7}$$

which can also be expressed as

$$\begin{aligned}\boldsymbol{\alpha}_2^n(k) &= \left[\boldsymbol{\alpha}_1^n(k) - \boldsymbol{x}_2(k+1)\right]/T_s\\ &= \left[\boldsymbol{\alpha}_1^n(k) - \boldsymbol{x}_2(k) - T_s\boldsymbol{x}_3(k)\right]/T_s\end{aligned}\tag{A8}$$

Compared with (21), the causality contradiction is avoided in the new second virtual control law vector in (A8). Hence, by substituting (A7) into (A6), $\Delta V_2^n(k)$ can be derived as

$$\begin{aligned}\Delta V_2^n(k) = \frac{\gamma_2}{2}&T_s^2\boldsymbol{e}_3^{nT}(k)\boldsymbol{e}_3^n(k)\\ &-\frac{1}{2}(\gamma_2-\gamma_1T_s^2)\boldsymbol{e}_2^{nT}(k)\boldsymbol{e}_2^n(k)-\frac{\gamma_1}{2}\boldsymbol{e}_1^T(k)\boldsymbol{e}_1(k)\end{aligned}\tag{A9}$$

For guaranteeing the term of ΔV_2^n to be negative definite, and ensuring the vector of $\boldsymbol{e}_3^n$ to converge to be zero, the next step must be constructed.

Step A3: In this step, a sliding-mode control method is designed after the two steps in the backstepping design procedure. Define a sliding-surface vector as

$$\boldsymbol{s}(k) = \boldsymbol{e}_3^n(k) + k_1\boldsymbol{e}_2^n(k)\tag{A10}$$

where k_1 is a positive constant. The control law vector of the proposed DTBSMC method is assumed to take the following form:

$$\boldsymbol{u}_f(k)=\boldsymbol{b}_n^{-1}[\boldsymbol{F}(k)-\rho\mathrm{sgn}(\boldsymbol{s}(k))-k_2\boldsymbol{s}(k)-\boldsymbol{e}_3^n(k)+k_1\boldsymbol{e}_2^n(k)] \tag{A11}$$

where sgn(·) represents the sign function; k_2 is a positive constant; and the term of $\boldsymbol{F}(k)$ can be expressed as

$$\begin{aligned}\boldsymbol{F}(k)=&-\boldsymbol{x}_3(k)+\boldsymbol{a}_n\boldsymbol{x}_2(k)-k_1\boldsymbol{x}_2(k)-k_1T_s\boldsymbol{x}_3(k)\\&+\boldsymbol{\alpha}_2^n(k)+k_1\boldsymbol{\alpha}_1^n(k-1)\end{aligned} \tag{A12}$$

Define the third Lyapunov function candidate as

$$V_3^n(k)=\frac{1}{2}\boldsymbol{s}^T(k)\boldsymbol{s}(k)+V_2^n(k) \tag{A13}$$

Moreover, the difference of $V_3^n(k)$ can be expressed as

$$\begin{aligned}\Delta V_3^n(k)=&\boldsymbol{s}^T(k)\left[\boldsymbol{b}_n\boldsymbol{u}_f(k)-\boldsymbol{F}(k)+\boldsymbol{d}_p(k)\right]\\&-\boldsymbol{s}^T(k)\boldsymbol{s}(k)-\frac{\gamma_1}{2}\boldsymbol{e}_1^T(k)\boldsymbol{e}_1(k)\\&-\frac{1}{2}(\gamma_2-\gamma_1T_s^2)\boldsymbol{e}_2^{nT}(k)\boldsymbol{e}_2^n(k)+\frac{\gamma_2}{2}T_s^2\boldsymbol{e}_3^{nT}(k)\boldsymbol{e}_3^n(k)\end{aligned} \tag{A14}$$

By substituting (A11) into (A14), one can obtain

$$\begin{aligned}&\Delta V_3^n(k)\\&\le-(1+k_2)\boldsymbol{s}^T(k)\boldsymbol{s}(k)-(1-\frac{\gamma_2}{2}T_s^2)\boldsymbol{e}_3^{nT}(k)\boldsymbol{e}_3^n(k)\\&\quad-\frac{1}{2}(\gamma_2-\gamma_1T_s^2-2k_1^2)\boldsymbol{e}_2^{nT}(k)\boldsymbol{e}_2^n(k)-\frac{\gamma_1}{2}\boldsymbol{e}_1^T(k)\boldsymbol{e}_1(k)\end{aligned} \tag{A15}$$

If the condition of $\|\boldsymbol{d}_p(k)\|<\rho$ is satisfied, and the coefficients of $0<k_1<\sqrt{(\gamma_2-\gamma_1T_s^2)/2}$ is selected, $\Delta V_3^n(k)$ is a negative-definite function. According to the Lyapunov stability theorem [34], the system stability of the proposed DTBSMC method can be guaranteed, and the corresponding condition is independent of the grid impedance. In addition, the error vectors of $\boldsymbol{e}_1$, $\boldsymbol{e}_2^n$ and $\boldsymbol{e}_3^n$ will asymptotically converge to zero, and it implies that the grid current can track the current reference signal ($\boldsymbol{x}_d$).

APPENDIX B

The design procedure of the backstepping control method is also divided into three steps. Because the backstepping structure is the same as the part of the proposed DTBSMC strategy, the derivation of the first two steps of the backstepping control method makes no difference (Step A1 and Step A2). The difference of the derivation is in the third step without using the SMC method as shown as follows.

Step B3: For ensuring the vector of $\boldsymbol{e}_3^n$ in (A9) can converge to zero, the third Lyapunov function candidate ($V_{3b}^n(k)$) for the backstepping control method is designed as

$$V_{3b}^n(k)=\frac{1}{2}\boldsymbol{e}_3^{nT}(k)\boldsymbol{e}_3^n(k)+V_2^n(k) \tag{B1}$$

Therefore, the difference of $V_{3b}^n(k)$ can be derived as

$$\begin{aligned}\Delta V_{3b}^n(k)=&\frac{1}{2}\boldsymbol{e}_3^{nT}(k+1)\boldsymbol{e}_3^n(k+1)-\frac{1}{2}\boldsymbol{e}_3^{nT}(k)\boldsymbol{e}_3^n(k)+\Delta V_2^n(k)\\=&\frac{1}{2}\left[\boldsymbol{x}_3(k+1)-\boldsymbol{\alpha}_2^n(k)\right]^T\left[\boldsymbol{x}_3(k+1)-\boldsymbol{\alpha}_2^n(k)\right]\\&-\frac{1}{2}\boldsymbol{e}_3^{nT}(k)\boldsymbol{e}_3^n(k)+\Delta V_2^n(k)\\=&\frac{1}{2}\left[\boldsymbol{x}_3(k)-\boldsymbol{a}_n\boldsymbol{x}_2(k)+\boldsymbol{b}_n\boldsymbol{u}_{fb}(k)-\boldsymbol{\alpha}_2^n(k)\right]^T\\&\times\left[\boldsymbol{x}_3(k)-\boldsymbol{a}_n\boldsymbol{x}_2(k)+\boldsymbol{b}_n\boldsymbol{u}_{fb}(k)-\boldsymbol{\alpha}_2^n(k)\right]\\&-\frac{\gamma_1}{2}\boldsymbol{e}_1^T(k)\boldsymbol{e}_1(k)-\frac{1}{2}(\gamma_2-\gamma_1T_s^2)\boldsymbol{e}_2^{nT}(k)\boldsymbol{e}_2^n(k)\\&-(1-\frac{\gamma_2}{2}T_s^2)\boldsymbol{e}_3^{nT}(k)\boldsymbol{e}_3^n(k)\end{aligned} \tag{B2}$$

Thus, the control law vector ($\boldsymbol{u}_{fb}$) of the backstepping control method can be designed as

$$\boldsymbol{u}_{fb}(k)=\boldsymbol{b}_n^{-1}\left[-\boldsymbol{x}_3(k)+\boldsymbol{a}_n\boldsymbol{x}_2(k)+\boldsymbol{\alpha}_2^n(k)\right] \tag{B3}$$

By substituting (B3) into (B2), one can obtain

$$\begin{aligned}\Delta V_{3b}^n(k)=&-\frac{\gamma_1}{2}\boldsymbol{e}_1^T(k)\boldsymbol{e}_1(k)-\frac{1}{2}(\gamma_2-\gamma_1T_s^2)\boldsymbol{e}_2^{nT}(k)\boldsymbol{e}_2^n(k)\\&-(1-\frac{\gamma_2}{2}T_s^2)\boldsymbol{e}_3^{nT}(k)\boldsymbol{e}_3^n(k)\end{aligned} \tag{B4}$$

As can be seen form (B4), $\Delta V_{3b}^n(k)$ is a negative-definite function, and the system stability of the backstepping control method can be guaranteed.

REFERENCES

[1] R. A. Fantino, C. A. Busada, and J. A. Solsona, "Observer-based grid-voltage sensorless synchronization and control of a VSI-LCL tied to an unbalanced grid," *IEEE Trans. Ind. Electron.*, vol. 66, no. 7, pp. 4972–4981, Jul. 2019.
[2] S. Jayalath and M. Hanif, "Generalized LCL-filter design algorithm for grid-connected voltage-source inverter," *IEEE Trans. Ind. Electron.*, vol. 64, no. 3, pp. 1905–1915, Mar. 2017.
[3] R. A. Fantino, C. A. Busada, and J. A. Solsona, "Optimum PR control applied to LCL filters with low resonance frequency," *IEEE Trans. Power Electron.*, vol. 33, no. 1, pp. 793–801, Jan. 2018.
[4] J. Dannehl, C. Wessels, and F. W. Fuchs, "Limitations of voltage-oriented PI current control of grid-connected PWM rectifiers with *LCL* filters," *IEEE Trans. Ind. Electron.*, vol. 56, no. 2, pp. 380–388, Feb. 2009.
[5] N. He, D. Xu, Y. Zhu, J. Zhang, G. Shen, Y. Zhang, J. Ma, and C. Liu, "Weighted average current control in a three-phase grid inverter with an LCL filter," *IEEE Trans. Power Electron.*, vol. 28, no. 6, pp. 2785–2797, Jun. 2013.
[6] R. N. Beres, X. Wang, F. Blaabjerg, M. Liserre, and C. L. Bak, "Optimal design of high-order passive-damped filters for grid-connected applications," *IEEE Trans. Power Electron.*, vol. 31, no. 3, pp. 2083–2098, Mar. 2016.
[7] A. Kouchaki and M. Nymand, "Analytical design of passive *LCL* filter for three-phase two-level power factor correction rectifiers," *IEEE Trans. Power Electron.*, vol. 33, no. 4, pp. 3012–3022, Apr. 2018.
[8] T. Liu, J. Liu, Z. Liu, and Z. Liu, "A study of virtual resistor-based active damping alternatives for LCL resonance in grid-connected voltage source inverters," *IEEE Trans. Power Electron.*, vol. 35, no. 1, pp. 247–262, Jan. 2020.
[9] Y. Guan, Y. Wang, Y. Xie, Y. Lang, A. Lin, and X. Wang, "The dual-current control strategy of grid-connected inverter with *LCL* filter," *IEEE Trans. Power Electron.*, vol. 34, no. 6, pp. 5940–5952, Jun. 2019.
[10] F. D. Freijedo, E. Rodriguez-Diaz, M. S. Golsorkhi, J. C. Vasquez, and J. M. Guerrero, "A root-locus design methodology derived from the Impedance/Admittance stability formulation and its application for LCL grid-connected converters in wind turbines," *IEEE Trans. Power Electron.*, vol. 32, no. 10, pp. 8218–8228, Oct. 2017.

[11] X. Wang, L. Harnefors, and F. Blaabjerg, "Unified impedance model of grid-connected voltage-source converters," *IEEE Trans. Power Electron.*, vol. 33, no. 2, pp. 1775–1787, Feb. 2018.
[12] D. Pan, X. Ruan, C. Bao, W. Li, and X. Wang, "Optimized controller design for *LCL*-type grid-connected inverter to achieve high robustness against grid-impedance variation," *IEEE Trans. Ind. Electron.*, vol. 62, no. 3, pp. 1537–1547, Mar. 2015.
[13] X. Li, J. Fang, Y. Tang, X. Wu, and Y. Geng, "Capacitor-voltage feed-forward with full delay compensation to improve weak grids adaptability of LCL-filtered grid-connected converters for distributed generation systems," *IEEE Trans. Power Electron.*, vol. 33, no. 1, pp. 749–764, Jan. 2018.
[14] J. Samanes, A. Urtasun, E. Gubia, and A. Petri, "Robust multisampled capacitor voltage active damping for grid-connected power converters," *Int. J. Electr. Power Energy Syst.*, vol. 105, pp. 741–752, Feb. 2019.
[15] L. Zhou, J. M. Guerrero, X. Zhou, Y. Chen, Z. Lv, Z. He, W. Wu, L. Yang, K. Yan, and A. Luo, "Inverter-current-feedback resonance-suppression method for LCL-type DG system to reduce resonance-frequency offset and grid-inductance effect," *IEEE Trans. Ind. Electron.*, vol. 65, no. 9, pp. 7036–7048, Sep. 2018.
[16] L. Yang and J. Yang, "A robust dual-loop current control method with a delay-compensation control link for LCL-type shunt active power filters," *IEEE Trans. Power Electron.*, vol. 34, no. 7, pp. 6183–6199, Jul. 2019.
[17] Q. Huang and K. Rajashekara, "Virtual RLC active damping for grid-connected inverters with LCL filters," in *Proc. IEEE Appl. Power Electron. Conf. Exposit. (APEC)*, Mar. 2017, pp. 424–429.
[18] Y. He, X. Wang, X. Ruan, D. Pan, X. Xu, and F. Liu, "Capacitor-current proportional-integral positive feedback active damping for *LCL*-type grid-connected inverter to achieve high robustness against grid impedance variation," *IEEE Trans. Power Electron.*, vol. 34, no. 12, pp. 12423–12436, Dec. 2019.
[19] H.-C. Chen, P.-T. Cheng, X. Wang, and F. Blaabjerg, "A passivity-based stability analysis of the active damping technique in the offshore wind farm applications," *IEEE Trans. Ind. Appl.*, vol. 54, no. 5, pp. 5074–5082, Sep./Oct. 2018.
[20] W. Qi, S. Li, S.-C. Tan, and S. Y. R. Hui, "Parabolic-modulated sliding-mode voltage control of a buck converter," *IEEE Trans. Ind. Electron.*, vol. 65, no. 1, pp. 844–854, Jan. 2018.
[21] H. Komurcugil, S. Ozdemir, I. Sefa, N. Altin, and O. Kukrer, "Sliding-mode control for single-phase grid-connected *LCL*-filtered VSI with double-band hysteresis scheme," *IEEE Trans. Ind. Electron.*, vol. 63, no. 2, pp. 73–864, Feb. 2016.
[22] Y. Wang and R.-J. Wai, "Adaptive power decoupling strategy for single-phase grid-connected converter," *IEEE Trans. Ind. Appl.*, vol. 55, no. 4, pp. 4275–4285, Jul./Aug. 2019.
[23] S. Arora, P. Balsara, and D. Bhatia, "Input–output linearization of a boost converter with mixed load (Constant voltage load and constant power Load)," *IEEE Trans. Power Electron.*, vol. 34, no. 1, pp. 815–825, Jan. 2019.
[24] J. J. Ge, Z. M. Zhao, and J. J. Li, "Backstepping control for active power filter with LCL filter," in *Proc. 2nd IET Renew. Power Gener. Conf. (RPG)*, 2013, pp. 1–4.
[25] P. Lin, C. Zhang, P. Wang, X. Li, J. Xiao, P. Tu, and C. F. Hoong, "A global robust output regulation method for grid-connected inverter with LCL filter in weak grid condition," in *Proc. 12th IEEE Conf. Ind. Electron. Appl. (ICIEA)*, Jun. 2017, pp. 1646–1651.
[26] J. Wu and Y. Lu, "Adaptive backstepping sliding mode control for boost converter with constant power load," *IEEE Access*, vol. 7, pp. 50797–50807, 2019.
[27] J. Davila, "Exact tracking using backstepping control design and high-order sliding modes," *IEEE Trans. Autom. Control*, vol. 58, no. 8, pp. 2077–2081, Aug. 2013.
[28] Y.-J. Liu, C. L. P. Chen, G.-X. Wen, and S. Tong, "Adaptive neural output feedback tracking control for a class of uncertain discrete-time nonlinear systems," *IEEE Trans. Neural Netw.*, vol. 22, no. 7, pp. 1162–1167, Jul. 2011.
[29] A. Y. Alanis, E. N. Sanchez, and A. G. Loukianov, "Real-time discrete backstepping neural control for induction motors," *IEEE Trans. Control Syst. Technol.*, vol. 19, no. 2, pp. 359–366, Mar. 2011.
[30] Y. Li, C. Yang, S. S. Ge, and T. H. Lee, "Adaptive output feedback NN control of a class of discrete-time MIMO nonlinear systems with unknown control directions," *IEEE Trans. Syst., Man, Cybern. B, Cybern.*, vol. 41, no. 2, pp. 507–517, Apr. 2011.
[31] A. Yazdani and R. Iravani, *Voltage-Sourced Converter in Power Systems: Modelling, Control, and Application*. New York, NY, USA: Wiley, 2010.
[32] D. G. Holmes and T. Lipo, *Pulse Width Modulation for Power Converters: Principles and Practice*. Piscataway, NJ, USA: IEEE Press, 2003.
[33] J. Yu, P. Shi, H. Yu, B. Chen, and C. Lin, "Approximation-based discrete-time adaptive position tracking control for interior permanent magnet synchronous motors," *IEEE Trans. Cybern.*, vol. 45, no. 7, pp. 1363–1371, Jul. 2015.
[34] K. J. Astrom and B. Wittenmark, *Adaptive Control*. Reading, MA, USA: Addison-Wesley, 1995.
[35] S. S. Ge, G. Y. Li, and T. H. Lee, "Adaptive NN control for a class of strict-feedback discrete-time nonlinear systems," *Automatica*, vol. 39, no. 5, pp. 807–819, May 2003.
[36] K. Jalili and S. Bernet, "Design of *LCL* filters of Active-Front-End two-level voltage-source converters," *IEEE Trans. Ind. Electron.*, vol. 56, no. 5, pp. 1674–1689, May 2009.
[37] *IEEE Recommended Practice and Requirements for Harmonic Control in Electric Power Systems*, IEEE Standard 519-2014, (Revision of IEEE Std. 519-1992), Jun. 11, 2014.
[38] K.-P. Huang, Y. Wang, and R.-J. Wai, "Design of power decoupling strategy for single-phase grid-connected inverter under nonideal power grid," *IEEE Trans. Power Electron.*, vol. 34, no. 3, pp. 2938–2955, Mar. 2019.
[39] S. G. Parker, B. P. McGrath, and D. G. Holmes, "Regions of active damping control for LCL filters," *IEEE Trans. Ind. Appl.*, vol. 50, no. 1, pp. 424–432, Jan./Feb. 2014.

YU WANG was born in Jiangsu, China, in 1991. He received the B.S. degree in electric engineering and automation from the Nanjing University of Information Science and Technology, Nanjing, China, in 2013, and the M.S. degree in electric engineering from the China University of Mining and Technology, Xuzhou, China, in 2017. He is currently pursuing the Ph.D. degree with the Department of Electrical Engineering and Computer Science, National Taiwan University of Science and Technology, Taipei, Taiwan. His current research interests include renewable energy generation systems and micro-grids.

RONG-JONG WAI (Senior Member, IEEE) was born in Tainan, Taiwan, in 1974. He received the B.S. degree in electrical engineering and the Ph.D. degree in electronic engineering from Chung Yuan Christian University, Chung Li, Taiwan, in 1996 and 1999, respectively.

From August 1998 to July 2015, he was with Yuan Ze University, Chung Li, Taiwan, where he was the Dean of General Affairs, from August 2008 to July 2013, and the Chairman of the Department of Electrical Engineering, from August 2014 to July 2015. Since August 2015, he has been with the National Taiwan University of Science and Technology, Taipei, Taiwan, where he is currently a Distinguished Professor, the Dean of General Affairs, and the Director of the Energy Technology and Mechatronics Laboratory. He is a chapter-author of *Intelligent Adaptive Control: Industrial Applications in the Applied Computational Intelligence Set* (Boca Raton, FL: CRC Press, 1998) and the co-author of *Drive and Intelligent Control of Ultrasonic Motor* (Tai-Chung, Taiwan, R.O.C.: Tsang-Hai, 1999), *Electric Control* (Tai-Chung, Taiwan, R.O.C.: Tsang-Hai, 2002), and *Fuel Cell: New Generation Energy* (Tai-chung, Taiwan, R.O.C.: Tsang-Hai, 2004). He has authored more than 170 conference papers, over 190 international journal articles, and 58 inventive patents. His research interests include power electronics, motor servo drives, mechatronics, energy technology, and control theory applications. The outstanding achievement of his research is

for contributions to real-time intelligent control in practical applications and high-efficiency power converters in energy technology. He is a Fellow of the Institution of Engineering and Technology (U.K.) and a Senior Member of the Institute of Electrical and Electronics Engineers (USA). He received the Excellent Research Award, in 2000, and the Wu Ta-You Medal and Young Researcher Award, in 2003, from the National Science Council, China. He was a recipient of the Outstanding Research Award, in 2003 and 2007, from the Yuan Ze University, China, the Excellent Young Electrical Engineering Award, and the Outstanding Electrical Engineering Professor Award, in 2004 and 2010, from the Chinese Electrical Engineering Society, China, the Outstanding Professor Award, in 2004 and 2008, from the Far Eastern Y. Z. Hsu-Science and Technology Memorial Foundation, Chnia, the International Professional of the Year Award, in 2005, from the International Biographical Centre, U.K., the Young Automatic Control Engineering Award, in 2005, from the Chinese Automatic Control Society, China, the Yuan-Ze Chair Professor Award, in 2007, 2010, and 2013, from the Far Eastern Y. Z. Hsu-Science and Technology Memorial Foundation, China, the Electric Category-Invent Silver Medal Award in 2007, the Electronic Category-Invent Gold and Silver Medal Awards, in 2008, the Environmental Protection Category-Invent Gold Medal Award, in 2008, the Most Environmental Friendly Award, in 2008, the Power Category-Invent Bronze Medal Award, in 2012, and the Electronic Category-Invent Gold and Silver Medal Awards, in 2015, from the International Invention Show and Technomart, Taipei, China, the University Industrial Economic Contribution Award, in 2010, from the Ministry of Economic Affairs, China, the Ten Outstanding Young Award, in 2012, from the Ten Outstanding Young Person's Foundation, China, the Taiwan Top 100 MVP Managers Award, in 2012, from MANAGER today magazine, China, the Outstanding Engineering Professor Award, in 2013, from the Chinese Institute of Engineers, China, the Green Technology Category-Scientific Paper Award, in 2014, from the Far Eastern Y. Z. Hsu-Science and Technology Memorial Foundation, China, the Scopus Young Researcher Lead Award-Computer Science, in 2014, from Taiwan Elsevier, the Outstanding Research Award, in 2016, 2018, and 2020, from the National Taiwan University of Science and Technology, China, and the Most Cited Researchers Award, in 2016 (field: electrical and electronics engineering).